

Chandra Grating Spectroscopy of the X-ray Binary 4U 1700-37 in a Flaring State

Bram Boroson

*Center for Space Research, Massachusetts Institute of Technology, Cambridge, MA 02138;
bboroson@space.mit.edu*

and

Saeqa Dil Vrtilek

*Harvard-Smithsonian Center for Astrophysics, 60 Garden Street, Cambridge, MA 02138;
svrtilek@cfa.harvard.edu*

and

Timothy Kallman and Michael Corcoran

*NASA Goddard Space Flight Center; Greenbelt, MD 20771 tim@xstar.gsfc.nasa.gov,
corcoran@barnegat.gsfc.nasa.gov*

ABSTRACT

Chandra X-ray Observatory grating spectra of the supergiant X-ray Binary 4U 1700-37 reveal emission lines from hydrogen and helium-like S, Si, Mg, and Ne in the 4–13 Å range. The spectrum also shows fluorescent lines from S, Si, and a prominent Fe K α line at 1.94Å. The lines contribute to the previously unaccounted “soft excess” in the flux in this range at orbital $\phi \approx 0.7$. The X-ray source was observed during intermittent flaring, and the strengths of the lines vary with the source state. The widths of the lines (FWHM \approx 1000 – 2000 km/s) can result from either Compton scattering or Doppler shifts. Power spectra of the hard X-rays show red noise and the soft X-rays and lines show in addition quasiperiodic oscillations (QPOs) and a power-spectral break. Helium-like triplets of Si and Mg suggest that the gas is not in a pure photoionization equilibrium. We discuss whether resonant scattering could affect the line ratios or whether a portion of the wind may be heated to temperatures $T \sim 10^6$ K.

1. Introduction

High Mass X-ray Binaries (HMXBs) consist of a compact object (a neutron star or black hole) accreting from an early type stellar companion. Stars of spectral types O and B typically drive stellar winds with mass loss rates of $10^{-7} - 10^{-5} M_{\odot} \text{ yr}^{-1}$, and a portion of this outflowing gas may be captured by the gravity of the compact object. Simple analytic expressions of gravitational capture (e.g. Bondi & Hoyle 1944) show that in some systems, the observed X-ray luminosity may be accounted for entirely by accretion of the wind. Other HMXBs, however, are probably powered by Roche lobe overflow leading to a gas stream and accretion disk. Even systems in which it is thought that wind accretion dominates are often close to filling their Roche lobes (Petterson 1978). As the surface of the primary star approaches the critical potential surface, there is probably a smooth transition between a stellar wind enhanced along the line between the stars and Roche lobe overflow (Friend & Castor 1982).

One of the earliest tools for understanding these systems, suitable for low resolution X-ray spectroscopy, was the examination of the orbital variation of the X-ray absorption. Buff & McCray (1974) pointed out that as an accreting compact object orbits a normal companion with a spherically symmetric stellar wind, the wind should absorb soft X-rays at all phases of the orbit. The amount of absorption should increase as the compact object falls behind the densest parts of the wind, close to eclipse ingress and egress. This technique has been used, for example, by Haberl, White, & Kallman (1989, hereafter HWK), who observed a binary orbit of 4U 1700-37 using *EXOSAT*. In this system, however, the absorption is not symmetric about orbital phase $\phi = 0.5$ (Branduari et al. 1978). HWK showed that the excess absorption at $\phi > 0.6$ could be explained by an accretion stream conveying 8% of the gas that accretes onto the compact object.

In addition to a gas stream, an “accretion wake”, a bow shock trailing the compact object, has also been invoked to explain X-ray absorption in several systems (Livio, Shara, & Shaviv 1979) and has been simulated numerically (Blondin et al. 1990).

Another structure the compact object may create within the wind is a “photoionization wake”, which results when the accelerating stellar wind crashes into gas ionized by the X-ray source. The ionized gas coasts, as it lacks the ions that accelerate the wind through resonance scattering of the stellar continuum (Fransson & Fabian 1980). Photoionization wakes are probably responsible for optical absorption lines from the primaries in Vela X-1 and 4U 1700-37 at $\phi > 0.5$. A gas stream or accretion wake could cover the compact object but not enough of the primary to explain the optical absorption (Kaper, Hammerschlag-Hensberge, & Zuiderwijk, 1994). Photoionization wakes appear in numerical simulations of X-ray sources embedded in stellar winds for a wide range of X-ray luminosities (Blondin

1994).

High resolution X-ray spectroscopy is emerging as a powerful diagnostic of conditions in HMXBs. An *ASCA* eclipse spectrum of the X-ray pulsar Vela X-1 showed emission lines that could be attributed to hydrogen-like and helium-like ionization stages of heavy elements (Si, Mg, and Ne, and possibly S, Ar, and Fe) as well as neutral fluorescence lines. The line strengths could be qualitatively understood through a model of photoionization of the stellar wind (Sako et al. 1999). *ASCA* observations of the HMXB pulsar GX 301-2 also showed fluorescent lines from Ne, Si, S, Ar, and Ca, as well as a 0.8 keV bremsstrahlung component that may be caused by shocks trailing the neutron star (Saraswat et al. 1996).

The new generation of X-ray telescopes, *Chandra*-AXAF and *Newton*-XMM, are confirming and expanding on the results suggested by *ASCA* and are revealing diverse new phenomena. Paerels et al. (2000) observed emission lines and radiative recombination features in the HMXB Cygnus X-3 with *Chandra*. Line ratio diagnostics suggest the emission lines are formed by X-ray photoionization of the stellar wind. Schulz et al. (2002b) observed the Vela X-1 lines with much higher resolution than with *ASCA* using *Chandra*, and resolved lines that could be used to diagnose the state of the emitting gas. The HMXB black hole candidate Cygnus X-1 shows variable emission and absorption features (Schulz et al. 2002a), and may reveal the presence of a wind focused by the gravity of the compact object (Miller et al. 2002). The superluminal jet source GRS 1915+105 shows absorption from H and He-like Fe (Lee et al. 2002), while SS 433 shows relativistically Doppler-shifted emission lines that provide density and temperature diagnostics for the gas in the jets (Marshall, Canizares, & Schulz, 2002).

A new dimension can be added to high resolution X-ray spectroscopy of HMXBs when line features are observed through times when the X-ray continuum is varying. Power spectra of X-rays from HMXBs typically reveal noise with a fractional rms variability of 20-30% (Belloni & Hasinger 1990). Quasiperiodic oscillations (QPOs) with mHz frequencies have been observed from X-ray pulsars such as LMC X-4 (Moon & Eikenberry 2001a) and Hercules X-1 (Moon & Eikenberry 2001b, Boroson et al. 2000). Observations of X-ray lines from a stellar wind with variable X-ray illumination can test photoionization models.

For this investigation, we focus on the supergiant X-ray binary 4U 1700-37, discovered with *Uhuru* (Jones et al. 1973). The X-ray source is eclipsed with a 3.41 day period by its companion HD 153919 (Penny et al. 1973, Hutchings et al. 1973), determined to be an O6.5Iaf star of $M_O = 52 \pm 2 M_\odot$ and $T_{\text{eff}} = 42,000$ K. Doppler shifts of lines from HD 153919 indicate an orbit that is nearly circular (Heap & Corcoran 1992). EXOSAT and BATSE have set an upper limit of $\approx 4\%$ on coherent pulsations near the expected ~ 100 s period of a typical X-ray pulsar (Doll & Brinkmann 1987, Rubin et al. 1996).

Corbet (1986) showed that most HMXB X-ray pulsars are either orbiting Be stars, or fall into separate period classes, $10^2 - 10^3$ s and 1-10 s, that may represent wind-fed and disk-fed systems, respectively. The few reported detections of pulsations in 4U 1700-37 have not been repeated. Murakami et al. (1984) reported 67.4 second pulsations during a flare observed with *Tenma*.

There is no consensus on the cause of the flares in 4U 1700-37. The X-ray light curve shows periods, lasting on the order of an hour, when the flux increases by up to a factor of ~ 10 . These flaring periods are accompanied by flickering in the light curve, also by about a factor of 10, on time scales of seconds to about 10 minutes. Brinkman (1981), based on a model of an entirely wind-accreting system, suggested that the flares were associated with accretion from the magnetotail of a neutron star. Tentative detection of pulsations suggested to Muakami et al. (1984) a similarity between 4U 1700-37 and LMC X-4, an X-ray pulsar that increases the fraction of pulsed X-rays during flares in which the X-ray luminosity can reach several times the Eddington luminosity. Levine et al. (2000) suggested three possible causes for the flares in LMC X-4: an accretion instability, fusion on the neutron star, or magnetic reconnection. In contrast to LMC X-4, in which the spectrum becomes softer during flares, the spectral changes during flares in 4U 1700-37 are not consistent, although there is evidence that the soft X-ray excess can increase during flares (HWK).

The lack of a clear detection of pulsations in 4U 1700-37 is surprising, as most neutron stars in HMXBs pulsate. The neutron stars in LMXBs are rarely pulsars, but they may have weaker magnetic fields owing to physical effects of accretion over the longer life of the system (Bhattacharya & Srinivasan 1995).

Measurements of the mass of the compact object in this system have been contradictory. The mass can be determined from the mass function of the O star,

$$f(M_O) \equiv PK_O^3(1 - e^2)^{3/2}/2\pi G = M_x \sin^3 i/(1 + 1/q)^2(1 - e^2)^{3/2} \quad (1)$$

where K_O is the orbital velocity of the O star, P is the orbital period, i is the inclination, $q = M_x/M_O$ is the mass ratio, and e is the eccentricity of the orbit. For K_O in km s⁻¹ and P in days this gives:

$$f(M_O) = 1.038 \times 10^{-7} K_O^3 P (1 - e^2)^{3/2} \quad (2)$$

Heap & Corcoran (1992) using $K_O = 18 \pm 3$ km s⁻¹, as determined from *IUE* observations, find $f(M_O) = 0.0023 \pm 0.0005 M_\odot$, resulting in an $M_x = 1.8 \pm 0.4 M_\odot$. Stickland & Lloyd (1993) re-examined the *IUE* spectra that led to this determination, recalibrated the wavelength scale, and found instead $K_O = 5 - 10$ km s⁻¹, leading conservatively to $f(M_O) = 0.00035 M_\odot$, providing an uncomfortably *low* mass for the compact object. Stickland and Lloyd raise the possibility that the measured UV line variations do *not* give the

radial orbital motion of the O star. Recently, Clark et al. (2002) using a measurement of $K_O = 20.6 \pm 1.0$ by Hammerschlag-Hensberge et al. (work not yet published that involves reanalysis of spectroscopic data) found $M_x = 2.44 \pm 0.27 M_\odot$, uncomfortably high for a neutron star but lower than expected for a black hole candidate.

We list the measured parameters of the system in Table 1, including the range of mass determinations for the compact object is in a close orbit ($a \sin i = 2.0 \pm 0.4 R_O$, where $R_O = 18 \pm 3 R_\odot$, Heap & Corcoran 1992).

2. Observations

The *Chandra* observations we report here took place on August 22-23, 2000. We scheduled the observation to coincide with the period before eclipse at $\phi = 0.65 - 0.8$, so that we could investigate the pre-eclipse absorption component and the soft excess. The *Chandra* observation was coordinated with simultaneous observations with the Rossi X-ray Timing Explorer (*RXTE*, Jahoda et al. 1996).

We used the High Energy Transmission Grating Spectrometer (HETGS, Canizares et al. 2000) aboard the Chandra X-ray Observatory (Weisskopf et al. 2002). We used the telescope’s “faint” data mode, with a timed readout every 3.24104 seconds. The HETGS includes both a Medium Energy Grating (MEG) and a High Energy Grating (HEG) giving overall a spectral range of 1-35Å, with a resolution of $\lambda/\Delta\lambda = 1400$ at 12 Å and $\lambda/\Delta\lambda = 180$ at 1.8 Å. The dispersed spectra were then detected with the ACIS-S linear array of CCD chips. The zeroth order undispersed spectrum was severely piled-up, and was not used in our analysis.

The observation was uninterrupted with a total exposure of 4.241×10^4 s, including a deadtime correction of 1%. Including photons in both the MEG and HEG, but excluding background, we detected 630,787 dispersed photons.

2.1. Light Curves and Spectra

We show a light curve for the combined HEG and MEG first order spectra in Figure 1. We have ignored photons near the wavelength of the Fe K line, where pileup may flatten the light curve during flares.

We have determined the orbital ephemeris from RXTE ASM data to be $T_0 = 50088.625 \pm 0.030$ MJD, $P_0 = 3.411625 \pm 2 \times 10^{-5}$ days, and $\dot{P}/P = -1.5 \pm 0.5 \times 10^{-6}$ yr⁻¹.

Along with the *Chandra* light curve, we also plot in red the 2–9 keV light curve as observed with the Proportional Counter Array (PCA) on board *RXTE*. We show only counts from the PCU 3 unit, which is the most reliable, although three PCUs were operating during most of the observation. The agreement between the *Chandra* and *RXTE* light curves is generally excellent, although the *RXTE* light curve appears systematically brighter near flare peaks. The *RXTE* observation extended 41.4 hours before the *Chandra* observation and 6.8 hours after. The peak count rate in the *RXTE* PCU 3 over the entire *RXTE* observation was about twice the peak count rate during the *Chandra* observations.

For further analysis we divided the *Chandra* observation period into three main segments (Figure 1), which we call Flaring (F), Quiescent (Q), and Ending (E). The Flaring period starts at the beginning of the *Chandra* observation and ends at MJD 51778.6296, when the Quiescent period begins. (These times are spacecraft times, not corrected to the solar system barycenter.) The Quiescent period ends at MJD 51778.7454, when the Ending period begins.

The division of the light curve into F, Q, and E periods is made empirically based on the count rate. The average *Chandra* count rates in the (F,Q,E) periods are (6.4,0.7,1.7) cts s⁻¹. However, as we discuss in §3, the absorbing column increases throughout the observation, so that the intrinsic luminosity is more similar during the F and the E periods than the count rate would indicate. From simple broad-band fits of the spectra to absorbed power law models (see §3.1), we find average X-ray luminosities in the (F,Q,E) periods are (1.1,0.2,0.8) × 10³⁶ erg s⁻¹ (corrected for absorption).

In Figure 2, we show the 1–10 Å *Chandra* spectra of 4U 1700–37 at each of the three periods of the observation. We have co-added HEG and MEG counts in the ±1 orders. The background is negligible and has not been subtracted. We have applied standard CIAO procedures for “destreaking” the ACIS chips, and have verified that the strong lines do not overlap with chip gaps. Although for display purposes we show the total counts in the ±1 orders of the MEG and HEG added together, we fit the models to each order and instrument in parallel, using corresponding response files. Fluorescence lines, notably an Fe K line near 1.94 Å, are prominent in both the F and E periods, and less prominent in the Q period.

High ionization lines due to H-like and He-like stages are also prominent in the 4–12 Å wavelength range. We identify these lines using House (1969), the analysis of lines in the Vela X-1 spectrum by Schulz et al. (2002b), and the XSTAR code (Bautista & Kallman 2001, Kallman & Bautista 2001).

3. Analysis

To process and select counts, we used CIAO (*Chandra* Interactive Analysis of Observations) software version 2.2.1.

We fit the continuum using the ISIS software package (Houck & Denicola 2000) and rebinning the spectra by factors of 20 so that each bin has enough counts to allow use of the χ^2 statistic. This analysis is described in §3.1.

To fit the spectral lines, we used the Sherpa spectral fitting tool. Instead of χ^2 , we use the C statistic (Cash 1979), which is appropriate when bins have few counts. We analyze the fluorescence lines in §3.2 and the high ionization lines in §3.3.

For the spectral response files, we used `acisheg1D1999-07-22rmfN0004.fits` for the HEG and `acismeg1D1999-07-22rmfN0004.fits` for the MEG. We created auxiliary response files (ARFs) using the CIAO task “fullgarf” for event files for each of the three periods of the observation (Flaring, Quiescent, and Ending).

3.1. Continuum Spectrum

The hard continuum was fit using a power law absorbed by cold gas (a “Wisconsin absorber”, Morrison & McCammon 1983). We need a second component to fit the soft X-ray continuum. We obtained adequate fits when we allowed for a second power law component with the same photon power law index but with a different normalization and behind a different column density. Such a component could arise from Compton scattering in the wind. Haberl & Day (1992) fit *Ginga* spectra of 4U 1700-37 to a similar model, and Haberl (1991) performed Monte-Carlo simulations of scattering of the 4U 1700-37 spectrum in a stellar wind.

Parameters describing the continuum fits to the F, FH, FL, Q, E, and EL states are shown in Table 2.

The average spectrum during the Ending period with our determination of continuum level and identification of spectral lines is shown in Figure 4.

3.2. Fluorescent Lines

We discuss the low-ionization fluorescence lines (Fe K, Ca, Ar, S, Si, and Mg, in order of increasing wavelength) observed with *Chandra*, paying special attention to the brightest

fluorescence feature, the Fe K line near 1.94 Å. In Figure 3 we show the spectrum in the region of the Fe K lines during the F, Q, and E periods, along with our model fit. The fit in Figure 3a of the Fe K lines during the Flaring period shows that the data are slightly in excess of the model. We note that the model is *not* fit to the summed data, but that the spectrum in each HETG arm is fit in parallel. The HEG +1 and –1 spectra show Fe K peaks offset by 0.005Å from each other

The Fe K line may be subject to some pileup during the Flaring period. Two photons with energies E_1 and E_2 striking the detector within a frame time register with an energy $E_1 + E_2$. While the number of piled up photons can in some cases be deduced from the ACIS-detected energy, the energy carried by piled-up Fe K photons would exceed the ACIS threshold. Pileup in the Fe K line in the Flaring period would not only lead to an underestimate of the flux in the line, but also an overestimate of the line width.

The edge apparent near 1.74Å in Figure 3c results from the neutral Fe K edge introduced by the “Wisconsin” model of interstellar absorption we use to fit the continuum (wabs).

Fitting the Flaring period spectrum to an absorbed power law plus Gaussian emission line gives a line centered at $1.937 \pm 0.002 \text{Å}$ (all errors are 90% confidence and are entirely determined from fitting) with a Full Width at Half Maximum (FWHM) of $2200 \pm 700 \text{km s}^{-1}$. During the Quiescent period, the centroid of the line is at a marginally longer wavelength, $1.940 \pm 0.002 \text{Å}$, with only an upper limit of 2200 km s^{-1} for the line width. During the Ending period, the line is centered on a wavelength of $1.936 \pm 0.001 \text{Å}$ but with a significantly narrower FWHM of $900 \pm 400 \text{ km s}^{-1}$.

To identify the ionization stages of Fe responsible for the line, we use the calculated $K\alpha$ line wavelengths of House (1969). We find that the 90% confidence range is compatible with Fe II–XII.

The most likely location for emission of the Fe K line is the stellar wind. HWK point out that the strength of the Fe K line seen in mid-eclipse with EXOSAT is consistent with the out of eclipse flux and the portion of the wind blocked by the normal star or not illuminated by X-rays during eclipse. However, the possibility remains that some fluorescent emission arises on an accretion disk or gas stream.

Motion of the stellar wind can introduce wavelength changes via the Doppler shift. Based on high resolution UV spectra obtained with *IUE*, Heap & Corcoran estimate a wind terminal velocity of $v_\infty = 2100 \text{ km s}^{-1}$, while van Loon et al. (2001) estimate a terminal velocity of $v_\infty = 1700 \text{ km s}^{-1}$ and a fractional microturbulent velocity of $\sigma = 0.15$, which leads to a similar Doppler broadening. However, we are not able to separate the effects of ionization stage, Doppler shift, and Compton scattering in the appearance of the emission

lines.

Comptonization can affect both the apparent wavelength of an emission line and its width (Kallman & White 1989). Ignoring the weak temperature dependence in the Comptonization broadening, the equations of Kallman & White, based on models of Podnyakov, Sobol, & Sunyaev (1979), Ross, Weaver, & McCray (1978), Langler, Ross, & McCray (1978), and Illarionov et al. (1978), imply that $\Delta\lambda/\lambda_0 = 0.0292\tau_{\text{Th}}$ where τ_{Th} is the optical depth for Thompson scattering. This implies $\tau_{\text{Th}} = 0.25 \pm 0.08$ for the flaring period and $\tau_{\text{Th}} = 0.10 \pm 0.05$ for the ending period. These values should be considered upper limits, as some line broadening could also result from a range of ionization stages in the emitting Fe or from Doppler shifts in the stellar wind, if the Fe K line is emitted in the wind.

Assuming such a τ_{Th} , and that the line centroid wavelength λ is shifted by Comptonization from the rest wavelength λ_0 according to $\lambda/\lambda_0 = 1 + 0.0375\tau_{\text{Th}}$ (as given by Kallman & White, ignoring the temperature correction), we find that our observations are compatible with all stages of Fe up to Fe XVIII. We emphasize that these limits are set by the centroid of the Fe K line and by its observed width.

The greatest scattering optical depth found from the line width, $\tau_{\text{Th}} = 0.25 \pm 0.08$, found during the Flaring period, corresponds to a column density $N_H = 3.8 \pm 1.2 \times 10^{23} \text{ cm}^{-2}$. The absorbing column density seen throughout the orbit varies from $\approx 4 \times 10^{22} \text{ cm}^{-2}$ from $\phi = 0.2$ to $\phi = 0.6$, and $2 - 4 \times 10^{23} \text{ cm}^{-2}$ from $\phi = 0.8 - 0.9$ (HWK 1989). Although EXOSAT did not observe from $\phi = 0.6 - 0.75$, the models of HWK predict a range of column densities of $N_H = 0.4 - 3 \times 10^{23} \text{ cm}^{-2}$. The scattering optical depth τ_{Th} decreases to $< 1.5 \pm 0.8 \times 10^{23} \text{ cm}^{-2}$ in the Ending period. Between the Flaring and Ending periods, the Fe K line is scattered by a *decreasing* column density, in anticorrelation with the absorbing column density, which *increases* between Flaring and Ending periods. This could be the result of the particular scattering geometry involved. The absorbing column density samples the wind along the line of sight from the X-ray continuum source, whereas the Fe K line is emitted in a more extended region in the wind (it persists through eclipse.)

During the F period, fits show only a marginal Fe K β line. However, the statistics are better during the E period, when the lines are narrower. We fit the K β line to a gaussian with central wavelength $\lambda = 1.755 \pm 0.003 \text{ \AA}$ and find a K β /K α ratio of 0.18 ± 0.09 (90% confidence), consistent with the theoretical value of ~ 0.13 for low optical depth in the lines (Kaastra & Mewe 1993).

The 5.36 \AA line which we attribute to SIV-VIII is absent in either of the low-luminosity states, as seen in Figure 5. There is marginal evidence for a line near 5.1 \AA in the Quiescent spectrum that is not present in the Ending state. This line could result from more highly

ionized sulfur.

We also examine the relation between the continuum flux level and the fluorescent line strength. We show in Figures 6 and 7 that overall the flux in the fluorescent lines increase approximately linearly with the continuum flux.

3.3. High Ionization Lines

The low energy (higher wavelength) lines, shown in Figure 4 are seen most prominently outside of the Flaring period, when the low-energy continuum has been diminished. The lines are similar to those seen by Schulz et al. (2002b) during X-ray eclipse in the wind-fed X-ray binary Vela X-1.

The flux in the low energy lines is sufficient to account for the “soft X-ray excess”, a feature of the X-ray spectrum previously without unique explanation. HWK attributed this excess mainly to the passage of the X-rays through a partially ionized absorber, but they found that this model could not account for the excess in the spectrum at $\phi > 0.6$. HWK attributed the much larger excess seen at these phases to scattering.

The line widths and centroid wavelengths are given in Table 4. The fluxes given are the observed fluxes of the lines, as they are behind an unknown column of absorbing gas. The errors in the line fluxes are probably overestimates, as they are based on the errors in the FWHM and line amplitudes, and these errors may be correlated.

These lines do not appear to be greatly variable as a result of either changes in orbital phase or the intermittent flares.

In Figure 5 we compare the low energy lines seen in the Flaring, Ending and Quiescent periods. We show only the spectrum during dips in the Flaring period, so that we can see the effect of the change in orbital phase. We have further subdivided the Ending period to separate periods in which the count rate was similar to the count rate in the Quiescent period. These time intervals are indicated by horizontal bars in Figure 1.

The low energy lines offer several diagnostics of the emitting gas. The Helium-like triplets of Si XIII and Mg XI are diagnostics of density and can be used to distinguish photoionization equilibrium from collisional ionization equilibrium (Porquet et al. 2002). These triplets consist of a forbidden line (f, with line strength z), two closely spaced intercombination lines (i, with strengths x and y), and a resonance line (r, with line strength w). We show the He-like Si triplet during the E period and the gaussian model in Figure 8.

The fits to the Si XIII lines (given in Table 4) give $(w, x + y, z) = (10 \pm 3, 3.8_{-1.8}^{+2.4}, 5.9_{-2.1}^{+2.6})$, where the errors are 90% confidence levels. This result is incompatible with the assumption of a purely photoionized plasma, which would have $z > w$, and instead suggests a low density hybrid between photoionized and collisionally ionized gas.

Anomalies in the He-like triplets in X-ray binaries are reported in Jimenez-Garate et al. (2002) and Wojdowski et al. (2002). Jimenez-Garate et al. suggested from Newton-XMM observations of Hercules X-1 that the f levels could be excited to the i levels by UV photons. However, this mechanism would not affect the r/f ratio. In addition, the wavelength of the UV photon required to raise Si XIII from the f to the i level is below the Lyman limit at 911Å, and would be absorbed before reaching far in the wind.

Wojdowski et al. analyze Chandra observations of Centaurus X-3 and find similar results to those presented here, namely a r/f ratio near unity, inconsistent with a purely photoionized gas. Wojdowski et al. suggest that photoionization equilibrium still holds, but that resonance scattering of the continuum by the r lines adds to their flux during eclipse, when the direct continuum is diminished by absorption. Outside of eclipse, however, one expects to see the r line superimposed with an absorption feature caused by scattering.

As can be seen in Figures 4 and 5, the ratio $r/f = w/z$ is $\gtrsim 1$ even in the low part of the Flaring period. This is centered near $\phi = 0.65$, far enough from eclipse that one might expect to see diminution of the r lines from an absorption trough. In §3.4, we discuss scattering scenarios in more detail.

The Mg XI triplet, seen in Figure 4b,c, is in the ratio $(w, x + y, z) = (6 \pm 3, 3 \pm 2, 4 \pm 2)$; unfortunately the error bars are larger than for Si, but the ratio is still consistent with a hybrid plasma.

3.4. Line Formation Models

We interpret the line strengths and ratios using the XSTAR photoionization code (Kallman & Bautista 2001, Bautista & Kallman 2001).

We used XSTAR version 2.1h, to compute the response of a gas to incident radiation. The results depend most strongly on the ionization parameter $\xi \equiv L/nr^2$, where L is the incident luminosity, n is the particle density, and r is the distance from the X-ray source, but also depend on the detailed source spectrum. We used a power law spectral shape with a high energy cut-off as determined from BeppoSax observations (Reynolds et al. 1999).

Our line models were motivated by the suggestion, from the line ratios in He-like Si, that

the gas was not entirely photoionized but that dynamical heating could play an important role as well. Fransson & Fabian for example show that a photoionization wake can form in a wind-fed X-ray binary, involving a collision of ionized gas and shadowed gas accelerated by the normal stellar wind mechanism. Temperatures 10^6 K can form over about a stellar radius at an angle of 45 degrees from the X-ray source.

Most low energy lines can be reproduced by a plasma fixed to temperature $T = 5 \times 10^6$ K and with an ionization parameter $\log \xi = 2$. Such models do not predict any prominent RRC features, consistent with the observations. For high temperatures, RRC features are broadened so that they are indistinguishable from continuum (although the absence of RRC features does not imply high temperature.)

However, concerns that temperatures reached in a photoionization wake might not be high enough to contribute to the ionization of the X-ray illuminated wind motivated us to study this problem further. A pure photoionization model could explain the anomalous He-like Si ratio through resonance scattering. Resonance scattering is a zero-sum process, and one might expect to have as many photons in the area scattered *away* as scattered *toward* the viewer. However, our point of view *is* special in that the inclination of the orbit is high; at the orbital phases of the *Chandra* observation, we may see the X-ray source through an enhanced-density gas stream. Our model of the continuum as including a Compton-scattered component that passes through a lower column density supports this.

If the gas is in pure photoionization equilibrium, it would have implications for how the X-ray lines change with the ionizing continuum.

Assuming pure photoionization, we have computed a Differential Emission Measure (DEM), a measure of the amount of gas at each bin of a parameter, usually temperature for work on stellar coronae in thermal equilibrium or ionization parameter ξ in environments like gas around X-ray binaries. The problem as typically stated is overdetermined, that is, there are more free parameters (for example, bins of $\log \xi$) than data points. However, a “penalty function” steers the solution toward one that is, for example, as smooth as possible. See Huenemoerder, Canizares, & Schulz (2001) for a more detailed description of the method. The major change we have introduced is to use the ionization parameter ξ instead of the temperature T .

When we allow values of $\log \xi$ from $\log \xi = 0$ to $\log \xi = 5$, and allow elemental abundances to be free parameters, we find that the DEM during the Ending period has two peaks, one at $\log \xi < 1$ (the emission of the Fe K line peaks at $\log \xi = 1 - 2$) and the other at $\log \xi \approx 4$.

If the only difference between the Quiescent and Ending period is the factor of ~ 4

increased luminosity in the Ending period, one would expect the DEM during the Q period to show a peak at $\log \xi = 3.4$ instead of the $\log \xi = 4$ peak in the E period. Thus one would expect emission lines formed at $\log \xi = 2$ to be *brighter* during the Q period than the E period. As a result, we would expect the Si XIV line, which has peak emissivity at $\log \xi = 3$, to be *dimmer* by a factor of 2 during the Ending period than the Quiescent period, when in fact we have observed the line to be 2.8 ± 0.7 times brighter in the Ending period. The change in the fluorescent lines between the E and Q periods is, however, consistent with the DEM. We find similar results when we freeze the elemental abundances to cosmic values. In this case, the DEM predicts that the Si XIV line would be 5 times brighter in the Q period.

Together with the anomalous He-like Si line ratios, this might suggest the gas is not in pure photoionization equilibrium. However, there are large systematic uncertainties in the method and possible complications in the physical picture. We suggest that if the anomalous He-like Si line ratio results from scattering, that further observations near $\phi = 0.5$ might reveal an absorption trough instead of emission in the Si XIII resonance line. Near $\phi = 0.5$, the gas stream is out of the line of sight to the X-ray source so that the 6-7Å continuum we see may be direct at not Compton scattered. The contribution of a resonance-scattered line component may be negligible against the direct continuum.

3.5. Power Spectra and Quasi-Periodic Oscillations

We created power spectra of both the overall count rate and the counts at wavelengths $\lambda > 4.5\text{\AA}$, displayed in Figure 9 and Figure 10, respectively. The power spectra are all Leahy-normalized (Leahy et al. 1983).

We fit the power spectrum of the integrated counts to an empirical model that consists of a power law with exponential cutoff, two Lorentzians, and a white noise component. With Leahy normalization, the white noise from counting statistics would be fixed at 2, but detector dead time can reduce this slightly, so the white noise level is left as a free parameter. We have binned the frequencies in the power spectra by a factor of 10 in order to determine errors in each bin. The reduced χ^2 value of our model of the power spectrum is $\chi^2_\nu = 1.4$.

One Lorentzian component, detected with marginal significance, may represent a quasiperiodic oscillation (QPO) with a centroid frequency of 6.5 mHz and a $Q = \nu/\Delta\nu$ value of ≈ 15 . This component represents a fractional rms power of 1.4%. In fact, there are several peaks in the 10^{-3} to 10^{-2} Hz range that may be QPO seen at low significance. Power spectral peaks with frequencies of exactly $1, 2 \times 10^{-3}$ Hz probably result from the spacecraft’s 1,000 second dither period.

The power spectrum of the region $\lambda > 4\text{\AA}$ shows more prominent QPO features (Figure 10). We also allow a third Lorentzian at the second harmonic of the 6.5 mHz QPO. The width of the second harmonic line is fixed to twice that of the fundamental. The fit gives $\chi^2_\nu = 2.1$, and it is clear that there are bumps in the 1–10 mHz range that the model does not account for. The 6.5 mHz line has a fractional rms amplitude of 4.5% while its second harmonic has an amplitude of 4.0%.

Similar temporal behavior has been seen from 4U 1700-37 before in the integrated counts observed with EXOSAT (Doll & Brinkmann 1987). Doll & Brinkmann argued that the timescales of variability in 4U 1700-37 reflected the flare recurrence rate and was linked to wind flow times.

Examination of the cross-correlation coefficient between the hard and soft X-rays shows a peak consistent with zero delay between the two.

We have also formed a power spectrum without any binning, in order to see more clearly the low frequency variations in the $\lambda > 4\text{\AA}$ spectrum. This power spectrum is displayed in Figure 11. To the eye there appears to be a cutoff near the frequency $\nu = 3 \times 10^{-4}$ Hz. The time scales of the cutoff and QPOs ($10^2 - 10^4$ seconds) lie between the light travel-time and wind-travel time between the stars. Our continuum models suggest that much of the flux in this wavelength range results from Compton scattering. The cutoff in the power spectrum could then result from smearing of the X-ray variability by Compton scattering.

Although the region $\lambda > 4\text{\AA}$ is dominated by lines during the Ending period (Figure 5), it is dominated by the continuum during the Flaring period (Figure 2). Thus the low frequency noise and stronger QPOs in the $\lambda > 4\text{\AA}$ region probably result from the continuum and not the lines. However, restricting analysis to only the wavelength regions surrounding the lines and to only the Quiescent and Ending periods, we still find significant low frequency noise.

4. Conclusions and Future Work

The current data set and the 4U 1700-37 system offer outstanding diagnostics of stellar winds and their disruption by compact objects.

The low energy lines (excluding the S line at 5.36Å and the Si line at 7.11Å) arise in highly ionized gas, yet a soft component is still visible through eclipse (HWK). XSTAR simulations can reproduce the low energy lines either in photoionization equilibrium with $\log \xi = 2.5 - 3.0$ or as a hybrid plasma at $T = 5 \times 10^6$ K with $\log \xi = 1.5 - 2.0$ (at the lower end of that range the Si XIV $\lambda 6.18$ to Si XIII $\lambda \lambda 6.64, 6.68, 6.74$ ratio becomes lower than observed).

In Figure 12 we show that for a uniform wind model, a region in photoionization equilibrium with $\log \xi = 2.5$ is smaller than the primary and would not be visible in mid-eclipse. While this would seem to support an extended region of hot gas (perhaps a photoionization wake) real stellar winds are probably highly nonuniform, with density contrasts of ~ 1000 . In such a nonuniform wind, there could be pockets of gas with $\log \xi = 2.5$ that extend all the way to the region indicated by $\log \xi = 0$ for the uniform wind case.

The Fe lines (and the low ionization $\text{S}\lambda 5.36$ and $\text{Si}\lambda 7.11$ lines) may arise in a region with $\log \xi \lesssim 1$. This region could be large enough for the lines to be visible through mid-eclipse even for a uniform wind.

Follow-up observations can test whether there is a variable delay between the hard and soft X-ray oscillations. This could result, for example, if the soft X-rays arise in a more extended region in response to hard X-rays from the compact object. During the present observations, we detected no delay.

QPO with mHz frequencies have been seen from a number of X-ray binary pulsars (Borison et al. 2000). The detection of mHz QPOs in 4U 1700-37 thus suggests that the compact object is a neutron star. Further observations, detecting QPOs at several X-ray luminosity states, can test any relationship between the frequency and an inner-disk radius.

The cause of the anomalous ratio in the Si XIII triplet has not been settled, but the two possible explanations, resonance scattering or a hybrid plasma, would both have important implications. The optical depth at 6.7\AA , and thus density in the wind would be constrained by the requirement that enough photons could be scattered. On the other hand, if the line ratios are caused by hot gas, this contributes evidence for and helps diagnose the physical extent and state of a photoionization wake.

One promising method for diagnosing resonance scattering is high resolution X-ray spectroscopy, but near $\phi = 0.5$, as described in §3.4.

If there is extended hot gas, we would expect it to contribute to the continuum emission. Such a component has been used to fit the continuum spectrum before. Haberl & Day (1992) used a bremsstrahlung component with $kT = 0.5$ keV behind a column density $N_H = 5 \times 10^{21} \text{ cm}^{-2}$ to fit *GINGA* spectra (as well as the *EXOSAT* data of HWK). ROSAT observations found a bremsstrahlung component with $kT = 0.47$ keV and $kT = 0.74$ keV after eclipse (Haberl, Aoki, & Mavromatakis, F., 1994). Most recently, BeppoSax observations found a $T = 0.2 \pm 0.1$ keV component (Reynolds et al. 1999). After adjusting the normalization of the HEG and MEG spectra, we find that we do not require a bremsstrahlung component to fit the broad-band spectrum during our *Chandra* observations. However, our models of

the broad-band continuum are hampered by uncertainties in the HEG and MEG effective areas, and a bremsstrahlung component may be present at flux levels lower than historically observed.

Other HMXB, such as Cen X-3 (Wojdowski et al. 2003) or Vela X-1 (Schulz et al. 2002) also show similar Si XIII diagnostics, but these have been interpreted to be result of resonance scattering. Given that Vela X-1 probably also has a photoionization wake (Kaper et al. 1994), emission from a hybrid plasma should also be considered as a possibility, particularly for that system. Again, analysis of observations at a variety of orbital phases can help distinguish between the possibilities. Hydrodynamic models of individual systems can also suggest whether the wind can be heated sufficiently by dynamical means.

SDV supported in part by NASA (NAG5-6711), and the Chandra X-ray Center (GO0-1100X). We would like to thank Mr. Andrew Beltz and Mr. Corey Casto for their assistance. We would like to thank the referee for comments.

Table 1. Parameters of the 4U 1700-37 System

Parameter name	Expression	Value	Reference ^a
Distance	D	1.9 kpc	1
Temperature of O star	T_*	$42000 \pm 2000, 35000 \pm 1000$ K	2, 4
O Star Radius	R_O	$18 \pm 3, 21.9^{+1.3}_{-0.5} R_\odot$	2, 4
Mass of O star	M_O	$52 \pm 2, 58 \pm 11 M_\odot$	2, 4
Mass of compact star	M_x	$1.8 \pm 0.4, 2.44 \pm 0.27 M_\odot$	2, 4
Spectral Type		O6.5Iaf	2
Orbital inclination	i	$> 80^\circ$	2
Orbital separation	$a \sin i$	$2.0 \pm 0.4 R_O$	2
Wind terminal velocity	v_∞	$2100 \pm 400, 1700$	2,3
Wind mass loss rate	\dot{M}	$6, 9.5 \times 10^{-6} M_\odot \text{ yr}^{-1}$	2, 4

^a1: Ankay et al. 2001, 2: Heap & Corcoran 1992, 3: van Loon et al. 2001, 4: Clark et al. 2002

Table 2. Fits to the X-ray Continuum

Parameter	F ^a	FH	FL	Q	E	EL
Exposure time (s) ^b	11420	6164	5256	10000	21531	3300
N_H (10^{23} cm^{-2})	$0.91^{+0.14}_{-0.07}$	$0.92^{+0.19}_{-0.12}$	$1.06^{+0.11}_{-0.06}$	1.27 ± 0.03	2.03 ± 0.08	$1.8^{+0.3}_{-0.1}$
Power Law Norm ^c	$0.16^{+0.03}_{-0.01}$	$0.17^{+0.04}_{-0.02}$	$0.18^{+0.06}_{-0.03}$	$0.038^{+0.020}_{-0.010}$	0.095 ± 0.018	$0.04^{+0.03}_{-0.02}$
Power Law γ ^d	$1.09^{+0.10}_{-0.07}$	$1.04^{+0.13}_{-0.08}$	$1.30^{+0.15}_{-0.11}$	$1.30^{+0.24}_{-0.13}$	1.00 ± 0.10	$1.2^{+0.4}_{-0.3}$
N_H (2) (10^{22} cm^{-2})	3.4 ± 0.5	$3.6^{+0.5}_{-0.4}$	2.0 ± 1.5	$0.29, < 3.9$	$0.95 (< 1.8)$	$0.97 (< 2.1)$
Power Law (2) Norm	$0.03^{+0.02}_{-0.01}$	$0.06^{+0.04}_{-0.02}$	$0.002^{+0.006}_{-0.001}$	$1.0 \pm 0.4 \times 10^{-4}$	$3^{+2}_{-1} \times 10^{-3}$	$4 \pm 2 \times 10^{-3}$
χ^2_ν, ν	1.06,607	1.15,301	1.13,357	1.09,61	1.07,301	(c-stat ^d ,61)

^aF=Flaring, FH=Flaring High, FL=Flaring Low, Q=Quiescent, E=Ending, EL=Ending Low, as shown in Figure 1

^bThe total on-source time, including non-readout time (“dead time”)

^cThe normalization is defined as the photons $\text{keV}^{-1} \text{ cm}^{-2} \text{ s}^{-1}$ at 1 keV.

^dThis is the “photon index”, so that the number of photons at energy E is given by $K(E/1\text{keV})^{-\gamma}$, where K is the normalization

^eFor the low ending state, we used the c-statistic (Cash 1979) instead of χ^2 , as even when the wavelength bins were grouped, the statistics were too poor to apply χ^2 .

Table 3. Measurements of Line Wavelengths, Widths, and Fluxes

λ (Å)	Mode ^a	Ion	λ_0 (Å) ^b	FWHM (km/s)	Flux (10^{-6} photons s^{-1} cm^{-2})
1.753±0.001	F	Fe II-XII,K β^c	1.756	2200±700	300±200
1.76±0.01	FH			2000±900	300±300
1.75±0.01	FL			2000±900	200±200
1.755±0.003	E			900±400	200±100
1.937±0.002	F	Fe II-XII,K α	1.936-1.937	2200±700	1200±200
1.937±0.002	FH			2000±900	1400±300
1.937±0.002	FL			2000±900	900±200
1.940±0.002	Q			< 2200	170±60
1.936±0.001	E			900±400	1100±90
1.938±0.001	EL			unresolved	350±130
3.355±0.001	E	Ca VI-VII	3.356-3.354	unresolved	46±15
4.18 ^d	F	Ar VI-IX	4.186-4.178	unresolved	40 ± 30
4.18 ^d	FL			unresolved	66±40
4.18 ^d	Q			unresolved	< 13
4.18 ^d	E	Ar VI-IX	4.186-4.178	unresolved	20±9
4.18 ^d	EL			unresolved	30 ⁺³⁰ ₋₂₀
4.744±0.004	F	S XVI	4.7274-4.7328	unresolved	60±30
4.744±0.002	FH			unresolved	90±50
4.69 ^{+0.05} _{-0.02}	FL			unresolved	30±30
4.74 ^d	E			unresolved	14 ± 7
4.74 ^d	EL			unresolved	< 22
5.10±0.01	Q	S XIII-XV	5.075-5.161	undetermined	14 ⁺¹² ₋₉
5.36 ^d	F	S IV-VIII	5.370-5.356	< 3000	50±30
5.366±0.005	FH			< 4000	80±50
5.36 ^d	FL			unresolved	40 ⁺⁴⁰ ₋₃₀
5.37±0.03	Q			> 1000	12±12
5.359±0.005	E			3000±1000	70±15
5.36±0.02	EL			3000	30 ⁺³⁰ ₋₂₀
6.17	F	Si XIV	6.199	unresolved	29±10
6.17	FH			unresolved	30±16
6.22±0.01	F	?		10000	30±14
6.22±0.01	FH	?		10000	47±25
6.17	FL			unresolved	27±11
6.18±0.01	Q			1800 ⁺¹⁸⁰⁰ ₋₇₀₀	6 ⁺⁴ ₋₃
6.177±0.003	E			1200±300	17±4
6.179±0.001	EL			1200	13 ⁺¹⁰ ₋₇
6.62±0.01	F	Si XIII	6.647	1900±500	38±12
6.61±0.02	FH			1200±500	39±19
6.633±0.006	FL			1000±500	25±10
6.63±0.01	Q			2000±1000	11 ⁺⁵ ₋₄
6.640±0.005	E			1200 ± 400	10 ± 3
6.640 ^d	EL			1200	10 ⁺⁹ ₋₆
6.68 ^{+0.07} _{-0.03}	Q	Si XIII	6.684,6.687	1400 ⁺¹⁵⁰⁰ ₋₆₀₀	1.9 ^{+3.0} _{-1.9}
6.684±0.009	E			1200±400 ^e	3.8 ^{+2.4} _{-1.8}
6.684 ^d	EL			1200	< 3
6.73±0.01	F	Si XIII	6.739	1900±500	33±12
6.73±0.01	FH			1200±500	43 ± 20
6.73±0.01	FL			1000±500	11 ⁺⁹ ₋₇
6.73±0.02	Q			2500 ⁺¹⁵⁰⁰ ₋₉₀₀	6 ⁺⁴ ₋₃

REFERENCES

- Ankay, A., Kaper, L., de Bruijne, J.H.J., Dewi, J., Hoogerwerf, R., Savonije, G.J. 2001, *A&A*, 370, 170
- Bautista, M.A., & Kallman, T.R. 2001, *ApJS*, 134, 139
- Belloni, T., & Hasinger, G. 1990, *A&A*, 230, 103
- Bhattacharya, D., & Srinivasan, G. 1995, in *X-ray Binaries*, ed. Walter H.G. Lewin, Jan van Paradijs, and Edward P.J. van den Heuvel, Cambridge University Press
- Blondin, J.M. 1994, *ApJ*, 435, 756
- Blondin, J.M., Stevens, I.R., & Kallman, T.R. 1991, *ApJ*, 371, 684
- Blondin, J.M., Kallman, T.R., Fryxell, B.A., & Taam, R.E. 1990, *ApJ*, 356, 591
- Bohlin, R.C. 1975, *ApJ*, 200, 402
- Bondi, H., & Hoyle, F. 1944, *MNRAS*, 104, 273
- Boroson, B., O'Brien, K., Horne, K., Kallman, T., Still, M., Boyd, P.T., Quaintrell, H., Vrtilek, S.D. 2000, *ApJ*, 545, 399
- Branduardi, G., Mason, K.O., Sanford, P.W. 1978, *MNRAS*, 185, 137
- Brinkmann, W. 1981, *A&A*, 94, 323
- Buff, J., & McCray, R. 1974, *ApJ*, 188, 37
- O'Brien, Kieran; Horne, Keith; Kallman, Timothy; Still, Martin; Boyd, Patricia T.; Quaintrell, Hannah; Vrtilek, Saeqa Dil
- Canizares, C.R., et al. 2000, *ApJ*, 539, L41
- Cash, W. 1979, *ApJ*, 228, 939
- Clark, J.S., Goodwin, S.P., Crowther, P.A., Kaper, L., Fairbairn, M., Langer, N., & Brockopp, C. 2002, *A&A*, 392, 909
- Corbet, R. 1986, *MNRAS*, 220, 1047
- Davidson, K., & Ostriker, J.P. 1973, *ApJ*, 179, 585
- Doll, H., & Brinkmann, W. 1987, *A&A*, 173, 86
- Fransson, C. & Fabian, A.A. 1980, *A&A*, 87, 102
- Friend, D.B., & Castor, J.I. 1982, *ApJ*, 261, 293
- Gehrels, N. 1986, *ApJ*, 303, 336
- Haberl, F., Aoki, T., & Mavromatakis, F. 1994, *A&A*, 288, 796

Table 3—Continued

λ (Å)	Mode ^a	Ion	λ_0 (Å) ^b	FWHM (km/s)	Flux (10^{-6} photons s^{-1} cm^{-2})
6.733±0.007	E	Si XIII	6.739	1200±200	5.9 ^{+2.6} _{-2.1}
6.733 ^d	EL			1200	< 8
7.05±0.06	F			13000 ⁺¹⁰⁰⁰⁰ ₋₄₀₀₀	50±20
7.00±0.11	FH	Si blend		8000 ⁺⁵⁰⁰⁰ ₋₃₀₀₀	120±40
7.09±0.04	FL			8000 ⁺⁵⁰⁰⁰ ₋₃₀₀₀	41±15
7.02±0.03	E	Si blend		8000 ⁺³⁰⁰⁰ ₋₂₀₀₀	12 ± 4
7.099±0.004	F	<Si VII	> 7.063	1100 ± 400	40±10
7.099±0.007	FH			1100 ⁺⁷⁰⁰ ₋₄₀₀	52±16
7.098±0.002	FL			800±400	32±10
7.110±0.007	Q			1700 ⁺¹²⁰⁰ ₋₇₀₀	14±5
7.110±0.003	E			1300±300	22 ± 4
7.110±0.01	EL			1300	13±7
7.84±0.02	E	Mg XI	7.850	2100 ⁺¹⁸⁰⁰ ₋₇₀₀	3±2
8.41 ^f	FH	Mg XII	8.419,8.424	< 1400	14±7
	FL			1100±500	13±6
	Q			< 8000	6±3
	E			1300±700	5 ± 2
9.1681	FH	Mg XI		3000 ⁺³⁰⁰⁰ ₋₁₀₀₀	21±10
	E			2500 ⁺²⁰⁰⁰ ₋₈₀₀	4 ± 2
9.2280	FH	Mg XI		3000 ⁺³⁰⁰⁰ ₋₁₀₀₀	< 10
	E			2500 ⁺²⁰⁰⁰ ₋₈₀₀	3 ± 2
9.3134	FH	Mg XI		3000 ⁺³⁰⁰⁰ ₋₁₀₀₀	< 14
	E			2500 ⁺²⁰⁰⁰ ₋₈₀₀	6 ± 3
10.238	FH	Ne X Ly β		unresolved	7 ⁺⁸ ₋₅
	E			unresolved	3±2
12.132	FH	Ne X Ly α		unresolved	8 ⁺¹⁰ ₋₆
	E			unresolved	4 ± 3

^aF=Flaring, FH=Flaring High, FL=Flaring Low, Q=Quiescent, E=Ending, EL=Ending Low, as shown in Figure 1

^bRest wavelength.

^cWe give wavelengths for $K\alpha_1$. The centroids are $\approx 0.002\text{\AA}$ greater than the α_1 wavelengths. The fluxes we give are for $K\alpha_1+K\alpha_2 = 1.5 K\alpha_1$

^dMarginal detection. The wavelength was frozen to the given value

^eThe He-like Si lines are fixed to have equal FWHM.

^fAll the lines with $\lambda > 8\text{\AA}$ have their wavelengths frozen to the given value

- Haberl, F., & Day, C.S. 1992, *A&A*, 263, 241
- Haberl, F., White, N.E., & Kallman, T.R. 1989, *ApJ*, 343, 409 (HWK)
- Hammerschlag-Hensberge, G., Howarth, I.D., & Kallman, T.R. 1990, *ApJ*, 352, 698
- Heap, S.R., & Corcoran, M.F. 1992, *ApJ*, 387, 340
- Houck, J. C & Denicola, L. A. 2000, *ASP Conf. Ser. 216: Astronomical Data Analysis Software and Systems IX*, 9, 591
- House, L.L. 1969, *ApJSS*, 155, 21
- Huenemoerder, D.P., Canizares, C.R., & Schulz, N.S., 2001, *ApJ*, 559, 1135
- Jahoda, K., Swank, J.H., Giles, A.B., Stark, M.J., Strohmayer, T., Zhang, W., Morgan, E.H. 1996, *SPIE*, 2808, 59
- Kaastra J.S. & Mewe, R. *A&AS*, 97, 443
- Kallman, T., & Bautista, M. 2001, *ApJS*, 133, 221
- Kaper, L, Hammerschlag-Hensberge, G., & Zuiderwijk, E.J. 1994, *A&A*, 289, 846
- Illarionov, A., Kallman, T.R., McCray, R.A., & Ross, R.R. 1978, *ApJ*, 228, 279
- Jimenez-Garate, M.A., Hailey, C.J., den Herder, J.W., Zane, S., & Ramsay, G. 2002, *ApJ*, in press
- Jones, C., Forman, W., Tananbaum, H., Schreier, E., Gursky, H., Kellogg, E., & Giacconi, R. 1973, *ApJ*, 181, L43
- Kallman, T., & White, N.E. 1989, *ApJ*, 341, 955
- Langer, S., Ross, R.R., & McCray, R.A. 1978, *ApJ*, 222, 959
- Leahy, D.A., Darbro, W., Elsner, R.F., et al. 1983, *ApJ*, 266, 160
- Lee, J., Reynolds, C.S., Remillard, R., Schulz, N.S., Blackman, E.G., Fabian, A.C. 2002, *ApJ*, 567, 1102
- Levine, A.M., Rappaport, S.A., Zojcheski, G. 2000, *ApJ*, 541, 194
- Livio, M., Shara, M.M., & Shaviv, G. 1979, *ApJ*, 233, 704
- Marshall, H.L., Canizares, C.R, Schulz, N.S. 2002, *ApJ*, 564, 941
- Miller, J.M., Wojdowski, P., Schulz, N.S., Marshall, H.L., Fabian, A.C., Remillard, R.A., Wijnands, R., & Lewin, W.H.G. 2002, *astro-ph/0208463*
- Murakami, T., Kawai, N., Makishima, K., & Mitani, K. 1984, *PASJ*, 36, 691
- Moon, D.-S., & Eikenberry, S.S. 2001a, *ApJ*, 549, 225
- Moon, D.-S., & Eikenberry, S.S. 2001b, *ApJ*, 552, 135

- Morrison, R., & McCammon, D. 1983, ApJ, 270, 119
- Nagase, F., Zylstra, G., Sonobe, Takashi, Kotani, T., & Inoue, H. 1994, ApJ, 436, L1
- Paerels, F., Cottam, J., Sako, M., Liedahl, D., Brinkman, A.C., van der Meer, R.L.J., Kaastra, J.S., Predehl, P. 2000, ApJ, 533, 135
- Petterson, J.A. 1978, ApJ, 224, 625
- Porquet, D., Mewe, R., Kaastra, J.S., Dubau, J., & Raassen, A.J.J. 2002, Proc. Symposium “New Visions of the X-ray Universe in the XMM-Newton and Chandra Era”, 26-30 November 2001, ESTEC, The Netherlands, in press.
- Pozdnyakov, L.A., Sobol, I.M., & Sunyaev, R.A. 1979, A&A, 75, 214
- Reynolds, A.P., Owens, A., Kaper, L, Parmar, A.N., & Sagreto, A. 1999, A&A 349, 873
- Ross, R.R., Weaver, R., & McCray, R.A. 1978, ApJ, 219, 292
- Rubin, B.C., Finger, M.H., Harmon, B.A., Paciesas, W.S., Fishman, G.J., Wilson, R.B., Wilson, C.A., Brock, M.N., Briggs, M.S., Pendleton, G.N., Cominsky, L.R., Roberts, M.S. 1996, ApJ, 459, 259
- Sako, M., Liedahl, D.A., Kahn, S.M., & Paerels, F. 1999, ApJ, 525, 921
- Saraswat, P., Yoshida, A., Mihara, T., Kawai, N., Takeshima, T., Nagase, F., Makishima, K., Tashiro, M., Leahy, D.A., Pravdo, S., Day, C.S.R., Angelini, L. 1996, ApJ, 463, 726
- Schulz, N.S., Cui, W., Canizares, C.R., Marshall, H.L., Lee, J.C., Miller, J.M., & Lewin, W.H.G., 2002a, ApJ, 565, 1141
- Schulz, N.S., Canizares, C.R., Lee, J.C., & Sako, M. 2002b, ApJ, 564, L21
- van Loon, J. Th., Kaper, L., & Hammerschlag-Hensberge, G. 2001, A&A 375, 498
- Weisskopf, M.C., O’Dell, S.L., & van Speybroeck, L.P. 1996, Proc. SPIE, 2905, 2
- Weisskopf, M.C., Brinkman, B., Canizares, C., Garmire, G., Murray, S., & Van Speybroeck, L.P. 2002, PASP, 114, 1
- Wojdowski, P.S., Liedahl, D.A., Sako, M., Kahn, S.M., & Paerels, F. 2002, ApJ, submitted

Fig. 1.— The combined MEG and HEG light curve of 4U 1700-37. We have divided the light curve into three separate intervals, which we call Flaring, Quiescent, and the Ending periods. To separate the effects of orbital phase and X-ray flaring, we investigate times in the F period when the X-ray light curve, smoothed over 30 pixels, is less than 30 cts per 3.24 second readout bin. We also investigate the spectrum during times in the E period in which the count rate resembles the count rate during the Q period. The separate intervals in the F and E periods that are selected for further analysis are indicated by the horizontal lines with bars at the ends. We overplot in red the contemporaneous RXTE light curve. The scale of the RXTE light curve is given on the right y axis.

Fig. 2.— The combined MEG and HEG spectrum of 4U 1700-37 integrated over the Flaring period (F), Quiescent period (Q), and Ending period (E) of our observation. The 1.93\AA Fe K line is apparent, as well as lines in the $4\text{-}8\text{\AA}$ range in the F and E spectra. The spectra have been binned to 0.04\AA resolution. We also show our model of the continuum, which consists of a power law behind two different column densities. The softer, less-absorbed spectrum is plotted with dashed lines, while the harder, more-absorbed component is plotted with dotted lines. The colors are chosen consistently within each observing segment (F,Q,E).

Fig. 3.— The Fe $K\alpha$ and $K\beta$ lines during the (a) Flaring ($0.005\text{ \AA}/\text{pixel}$), (b) Quiescent ($0.01\text{ \AA}/\text{pixel}$), and (c) Ending ($0.005\text{ \AA}/\text{pixel}$ binning) periods. The solid curve is the model fit, while the histogram is the combined MEG and HEG data. The edge near 1.74\AA results from neutral iron and is implicit in the model for cold absorption that the continuum (power law) passes through.

Fig. 4.— The $1.5\text{-}13\text{\AA}$ spectrum during the Ending period, with Gaussian fits to the lines and line identifications. We show (a) the count spectrum, (b) the log of the count spectrum, (c) the spectrum with the continuum model subtracted.

Fig. 5.— A comparison of the MEG spectra (in counts per second per 0.02 \AA bin) at different times. From top to bottom, the panels show: the spectrum during the low count rate intervals of the Flaring period, the spectrum integrated over the entire Quiescent period, the spectrum integrated over the entire Ending period, and the spectrum during the low count rate intervals of the Ending period. The error bars show the 1σ errors for the 7.1\AA line peak. The times of the low count rate periods are indicated by the horizontal bars in Figure 1.

Fig. 6.— Correlations between the flux in the X-ray continuum ($1\text{-}13\text{\AA}$) and the flux measured in fluorescent lines. For the continuum flux, we include both the direct and Compton-scattered components at the periods (FH,FL,Q,E,EL). a),b),c),d), and e) denote whether the fluorescence feature is due to Fe K, Ar, S, narrow Si near 7\AA , or broad Si near 7\AA . All

error bars are 90%

Fig. 7.— This is identical to the previous plot, but now the continuum includes only the hard component but without any absorption. Again, the fluorescence feature is caused by a) Fe K, b) Ar, c) S, d) narrow Si near 7\AA , or e) broad Si near 7\AA .

Fig. 8.— The spectrum near the He-like Si-triplet in the Ending period. The rest wavelengths of the Resonance, two Intercombination lines, and the Forbidden lines are shown with vertical dotted lines.

Fig. 9.— The Leahy-normalized power spectrum of the continuum. We have subtracted counts in the low energy lines from the total counts in HEG and MEG 1st order. The total model and individual model components are also shown. We show error bars where the logarithmic scale allows them to be visible.

Fig. 10.— The Leahy-normalized power spectrum of the low energy region. The total model and individual model components are also shown.

Fig. 11.— The Leahy-normalized power spectrum. In order to emphasize the low-frequency behavior, we have not performed any binning.

Fig. 12.— Contours of constant ionization parameter $\log \xi$ for a simple model of a uniform wind with $\dot{M} = 6 \times 10^{-6} M_{\odot} \text{ yr}^{-1}$, a terminal velocity of $v_{\infty} = 1700 \text{ km/s}$, a wind velocity law of $v(R) = v_{\infty}(1 - R_O/R)^{\beta}$ where $\beta = 0.8$. The “x” marks the position of the compact object and the circle shows the primary. The $\log \xi = 0.0$ ionization boundary is cut off where the primary’s shadow prevents X-rays from reaching the wind.

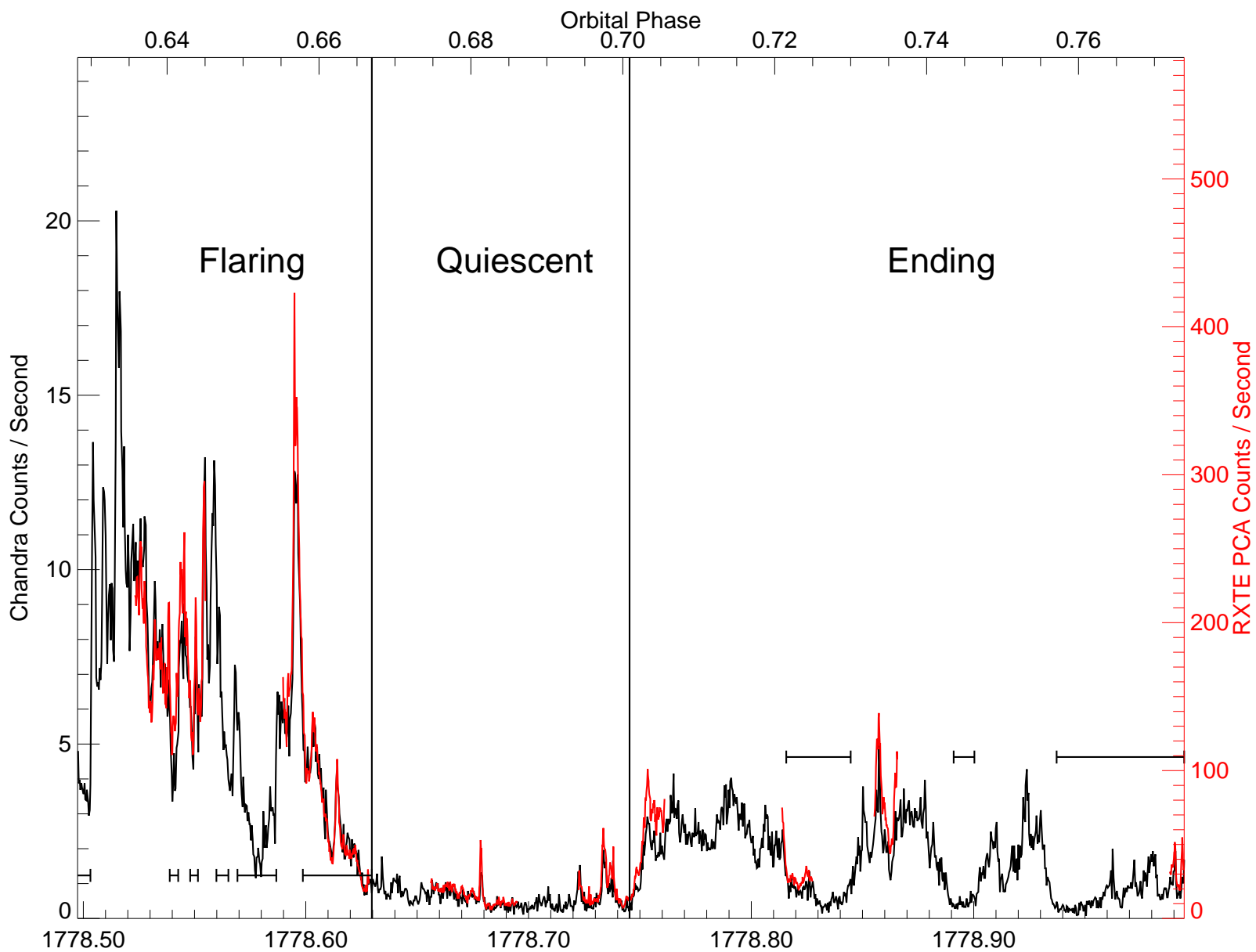


Fig. 1.—

Fig. 2.—

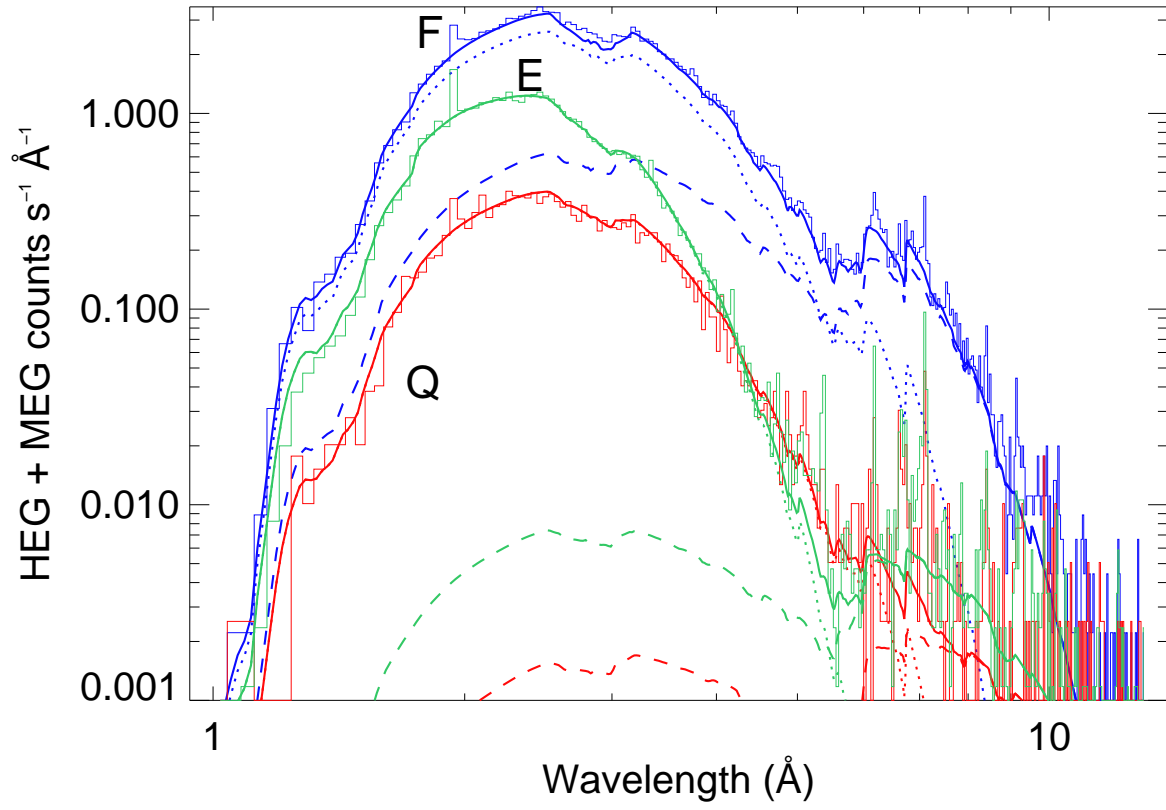
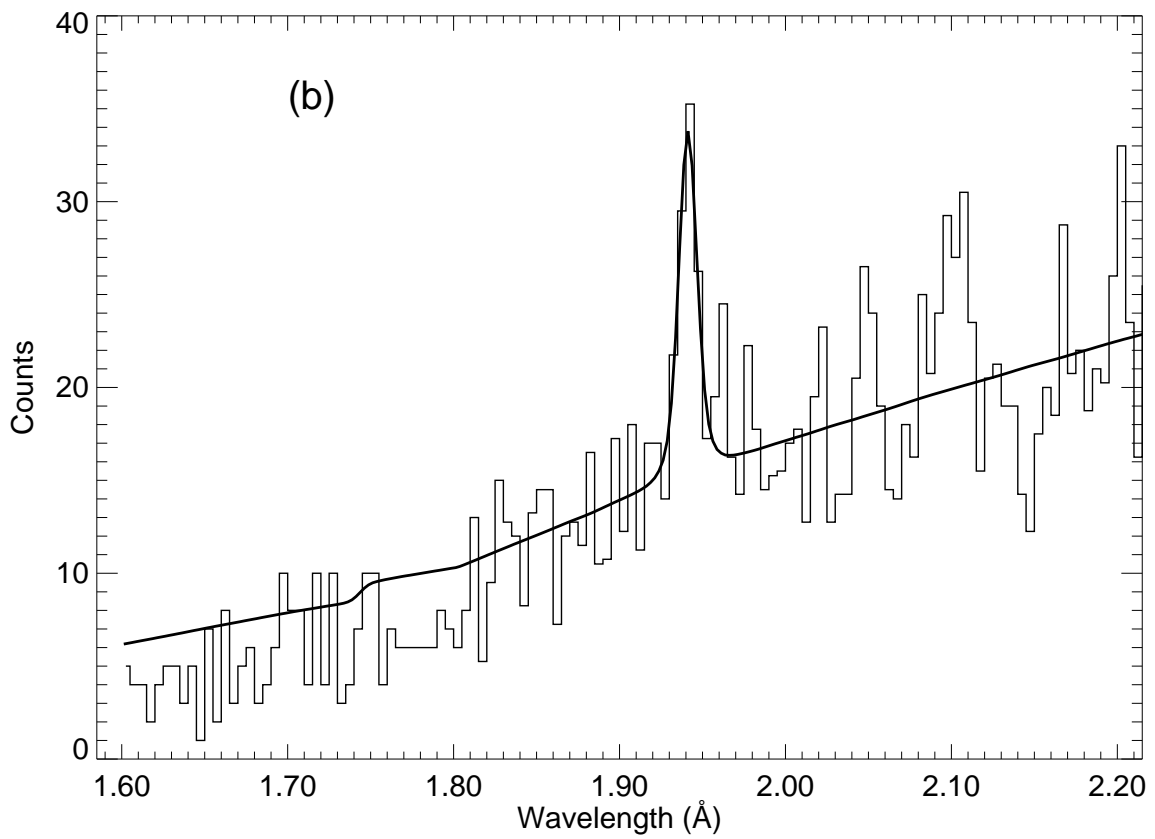
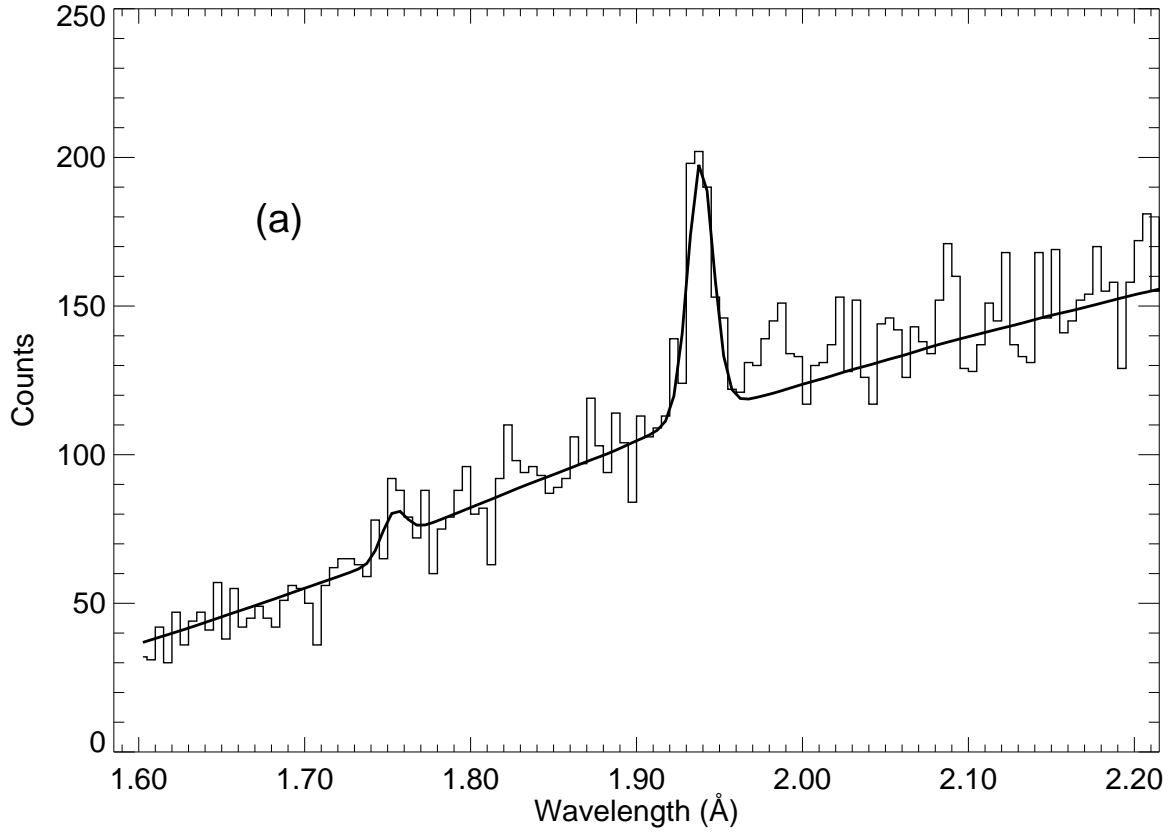


Fig. 3.—



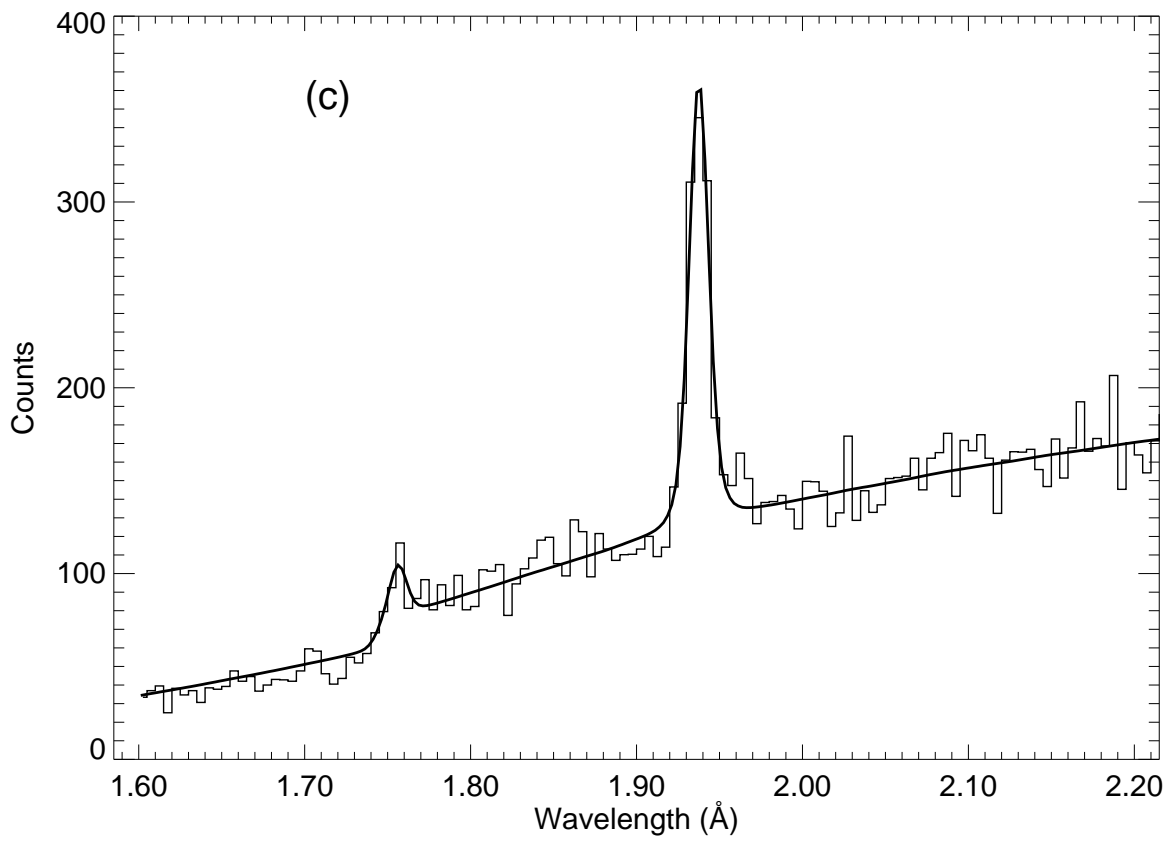
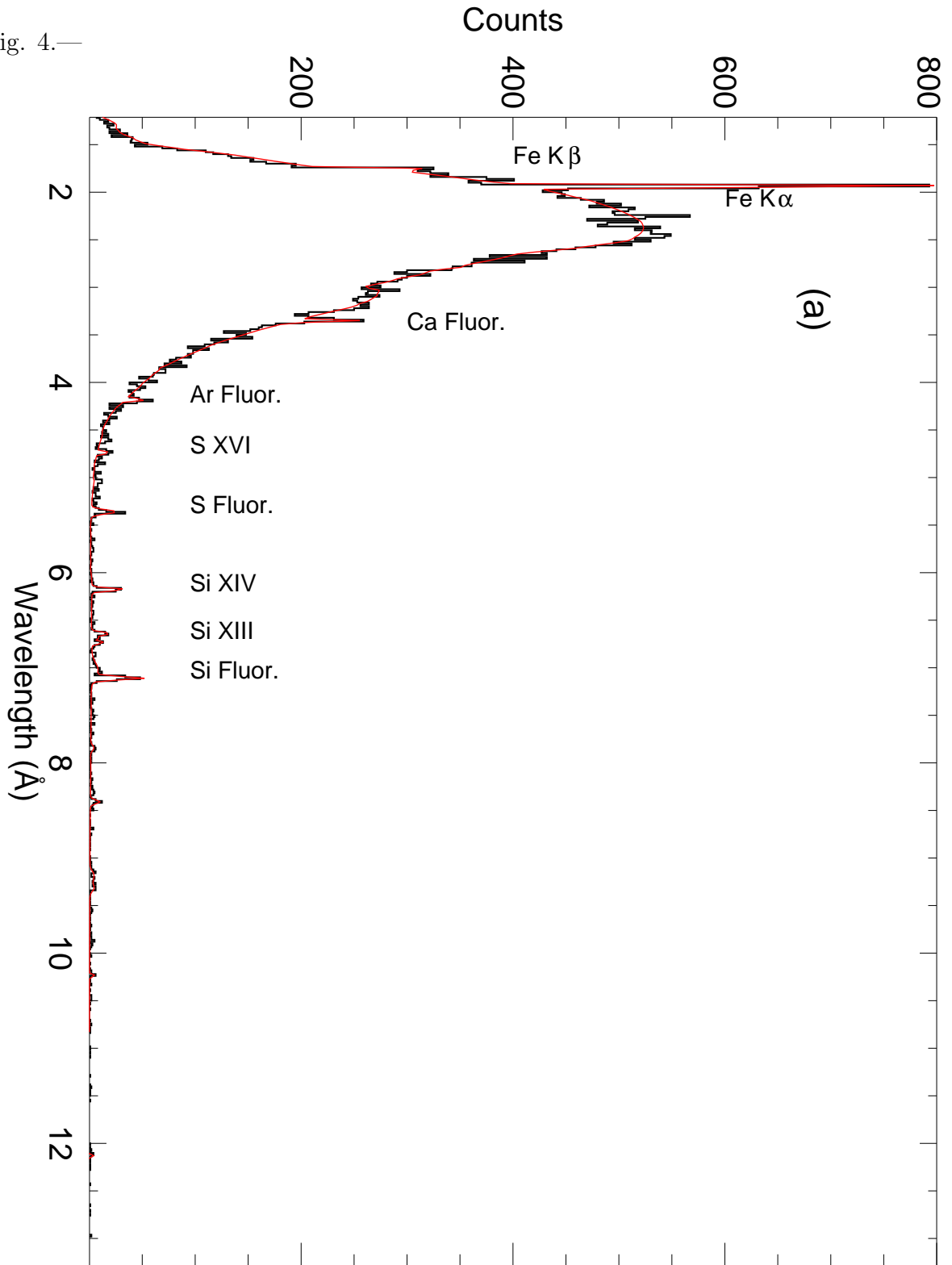
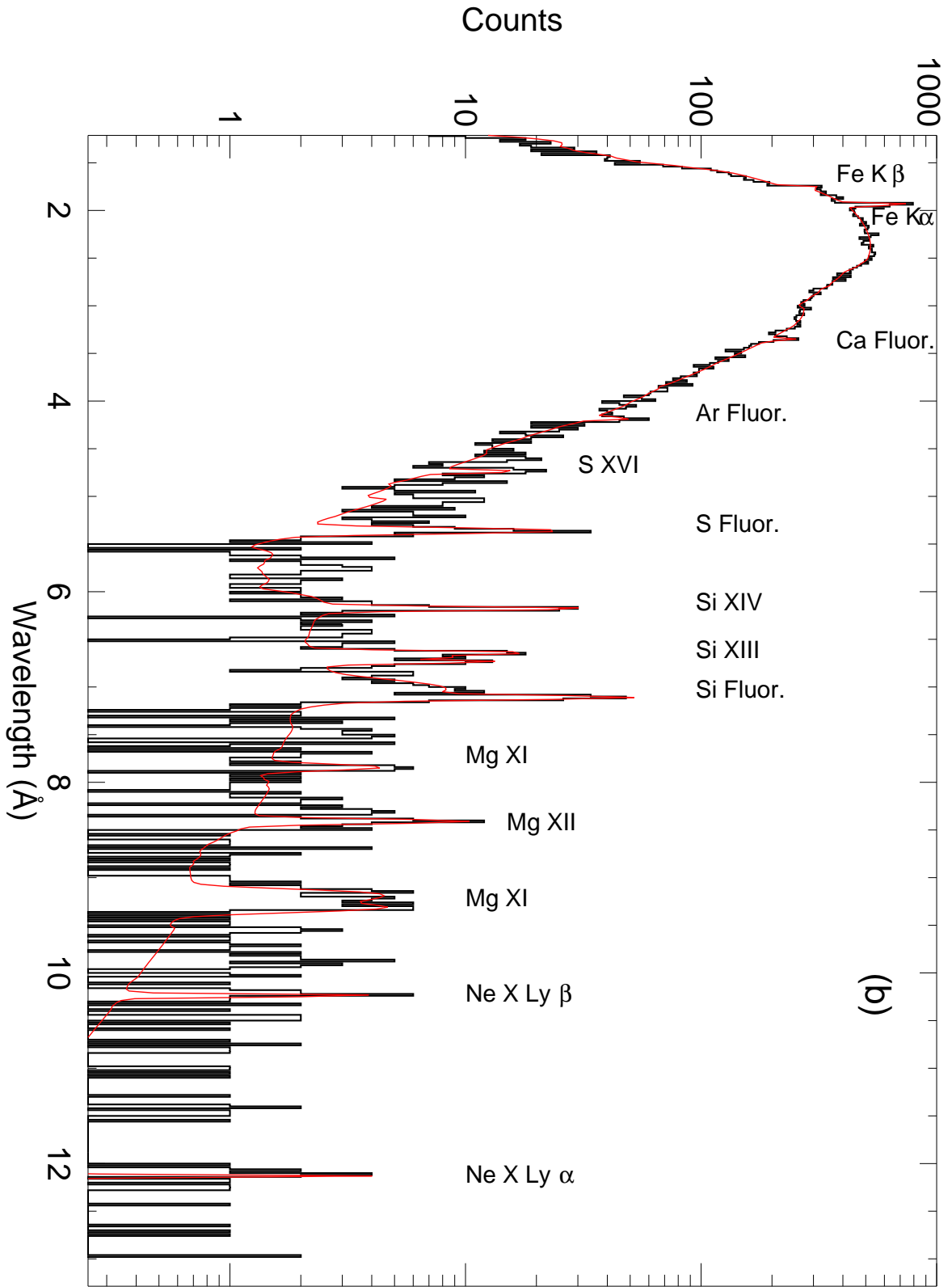


Fig. 4.—





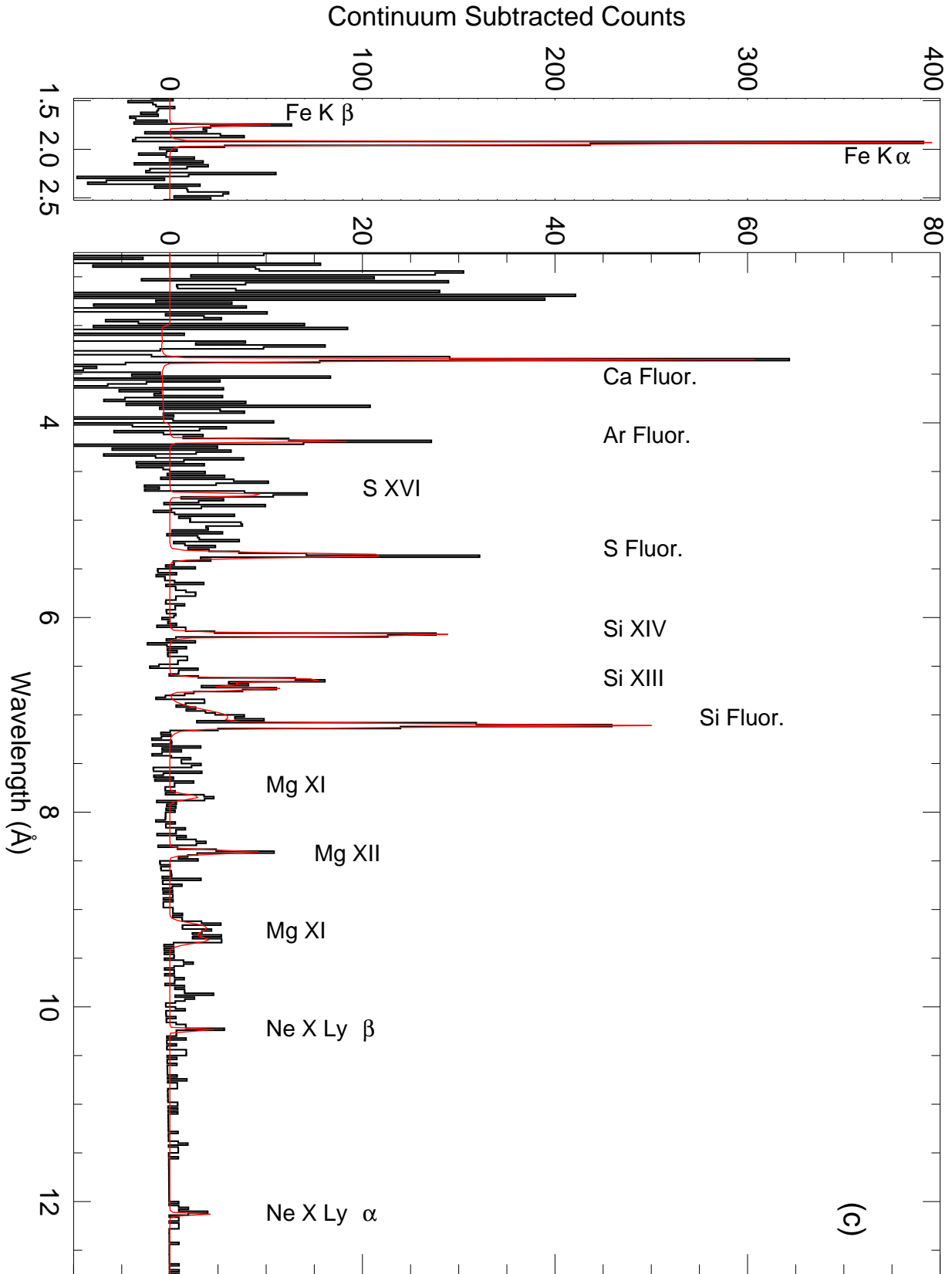


Fig. 5.—

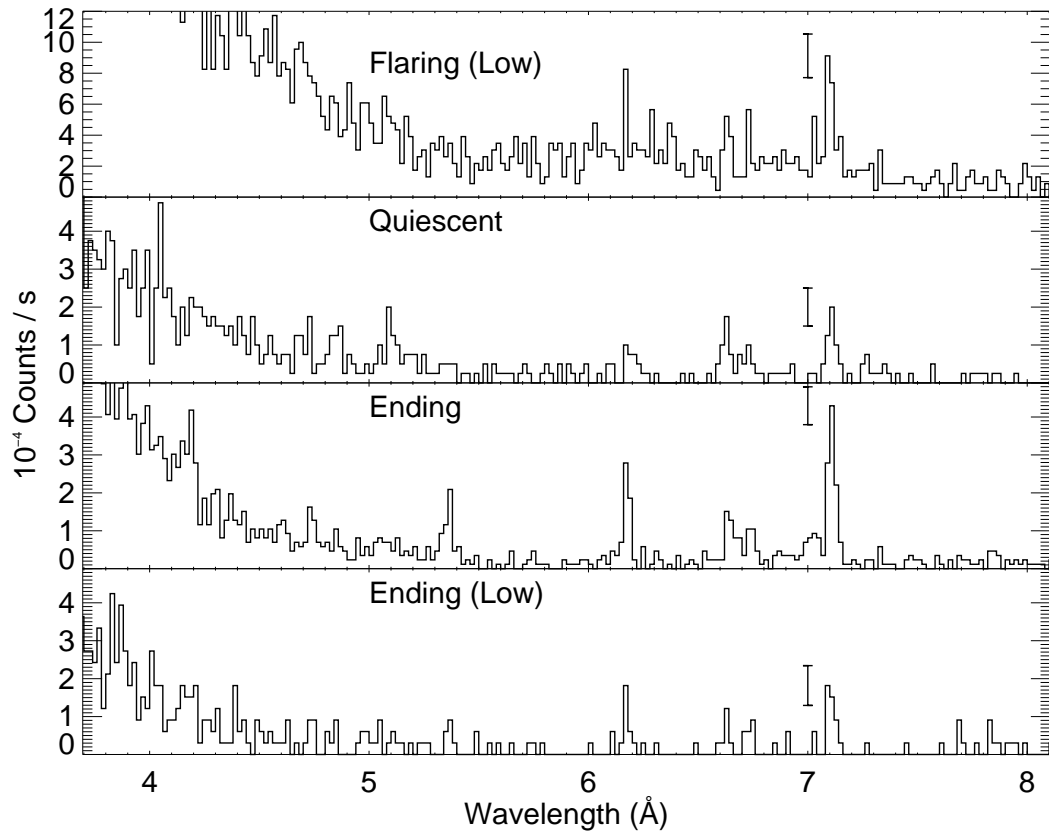
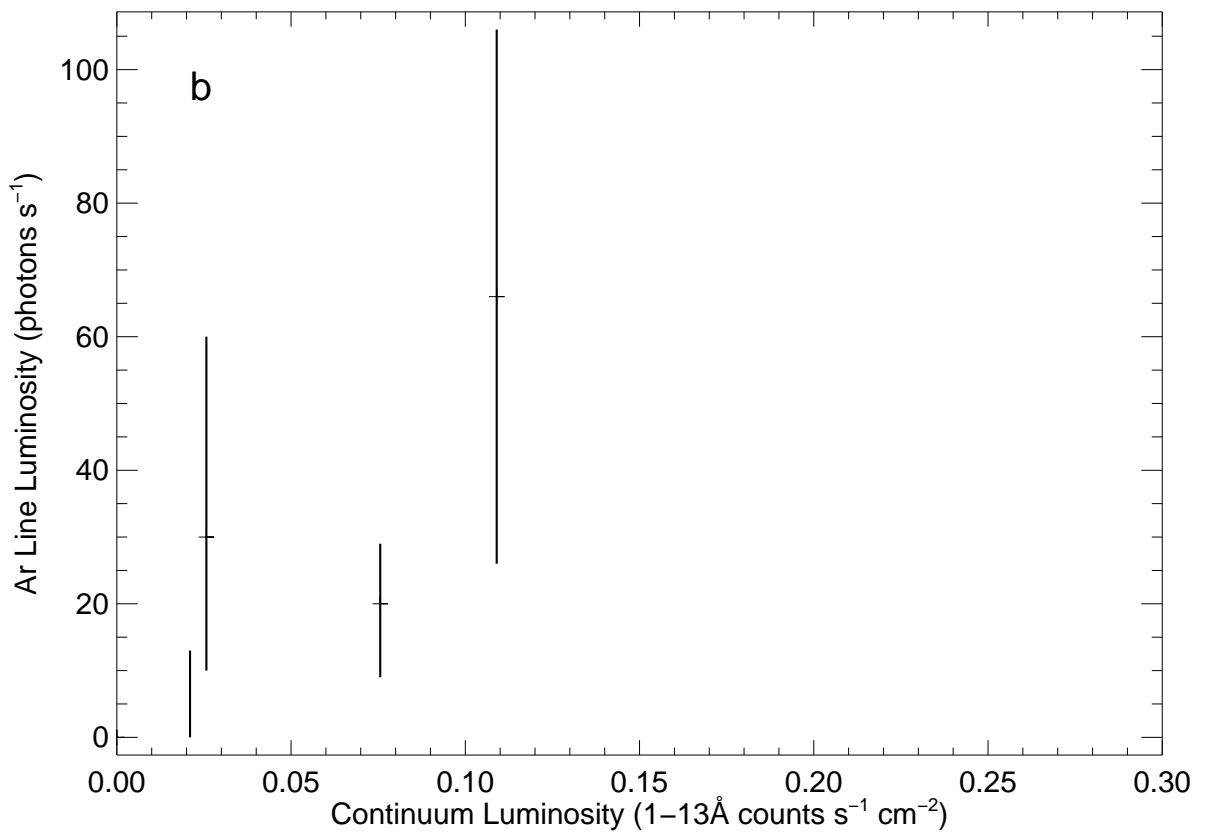
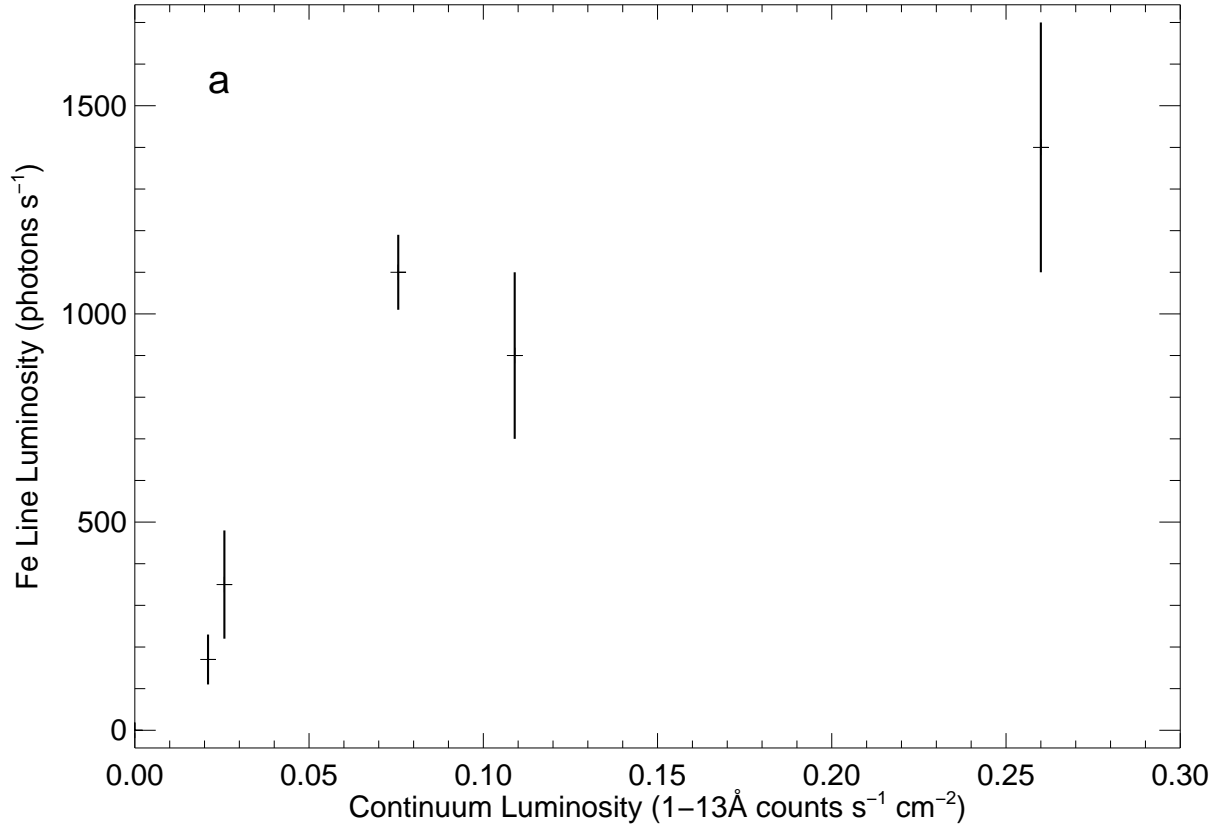
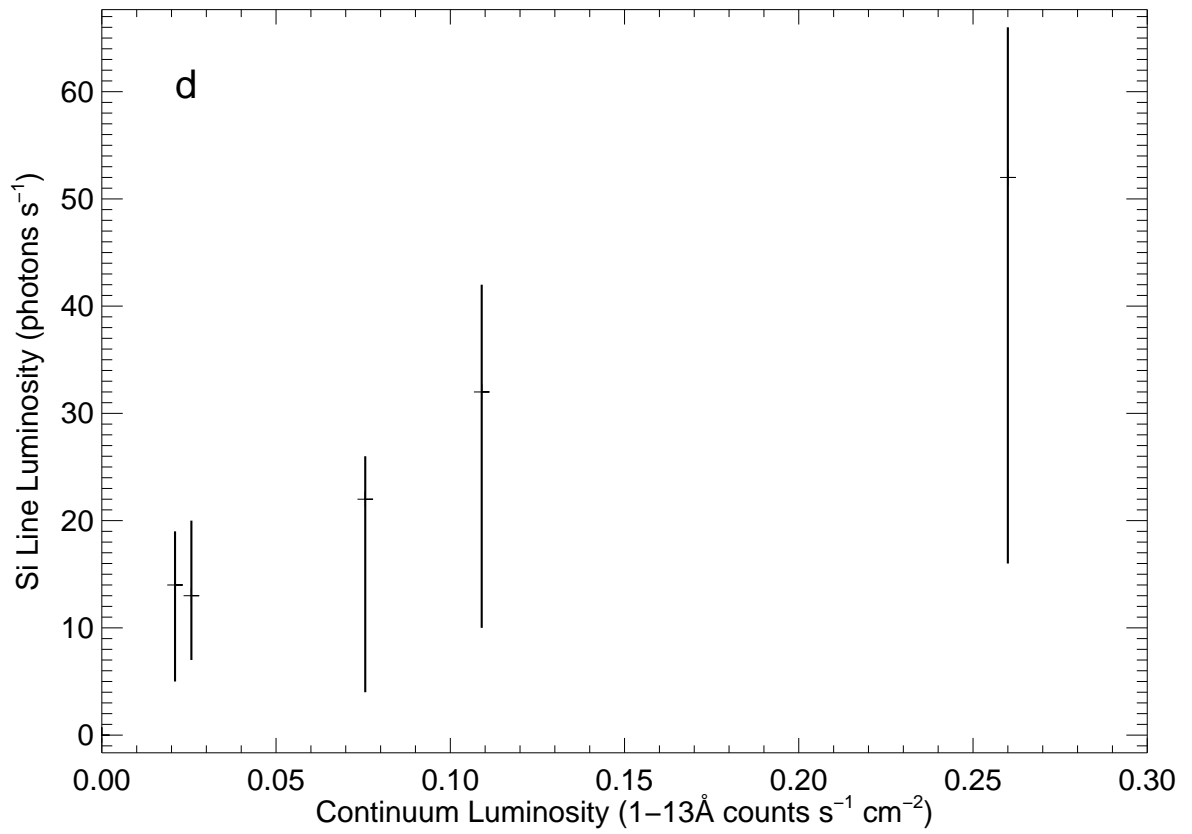
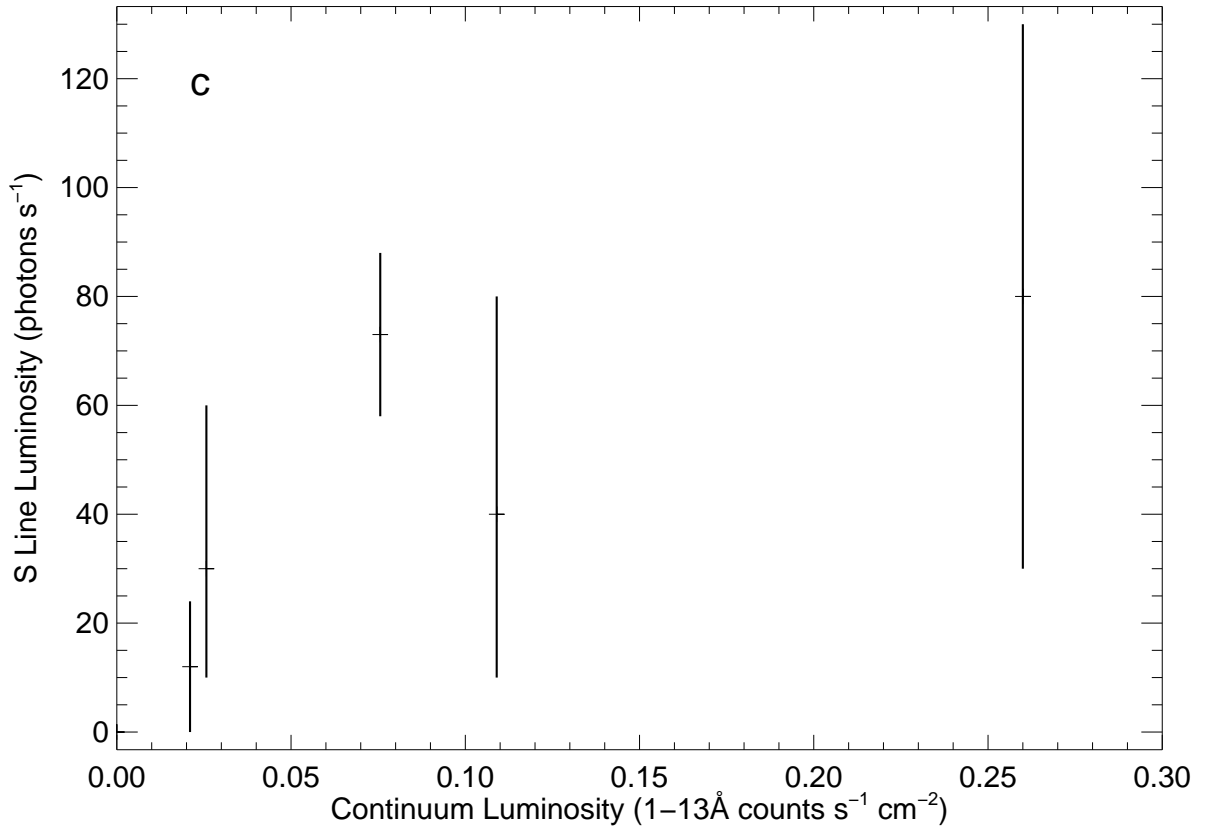


Fig. 6.—





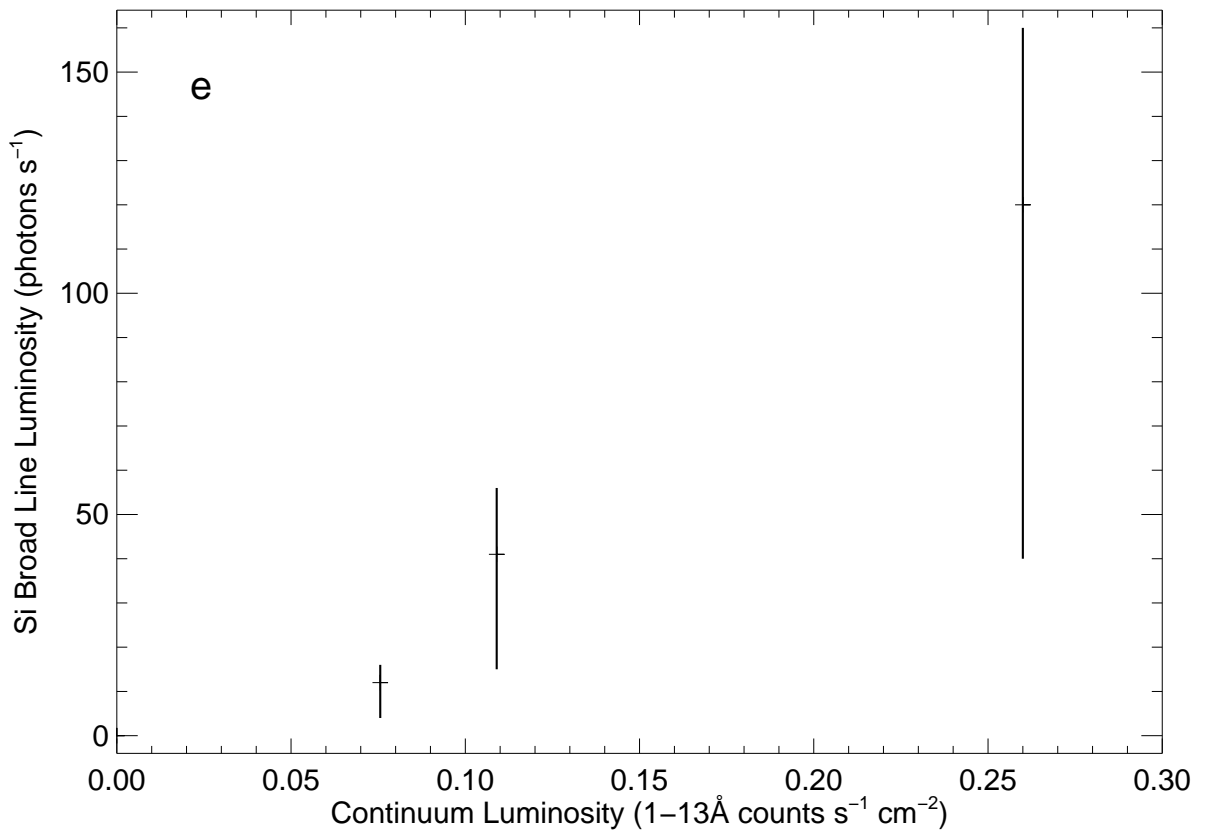
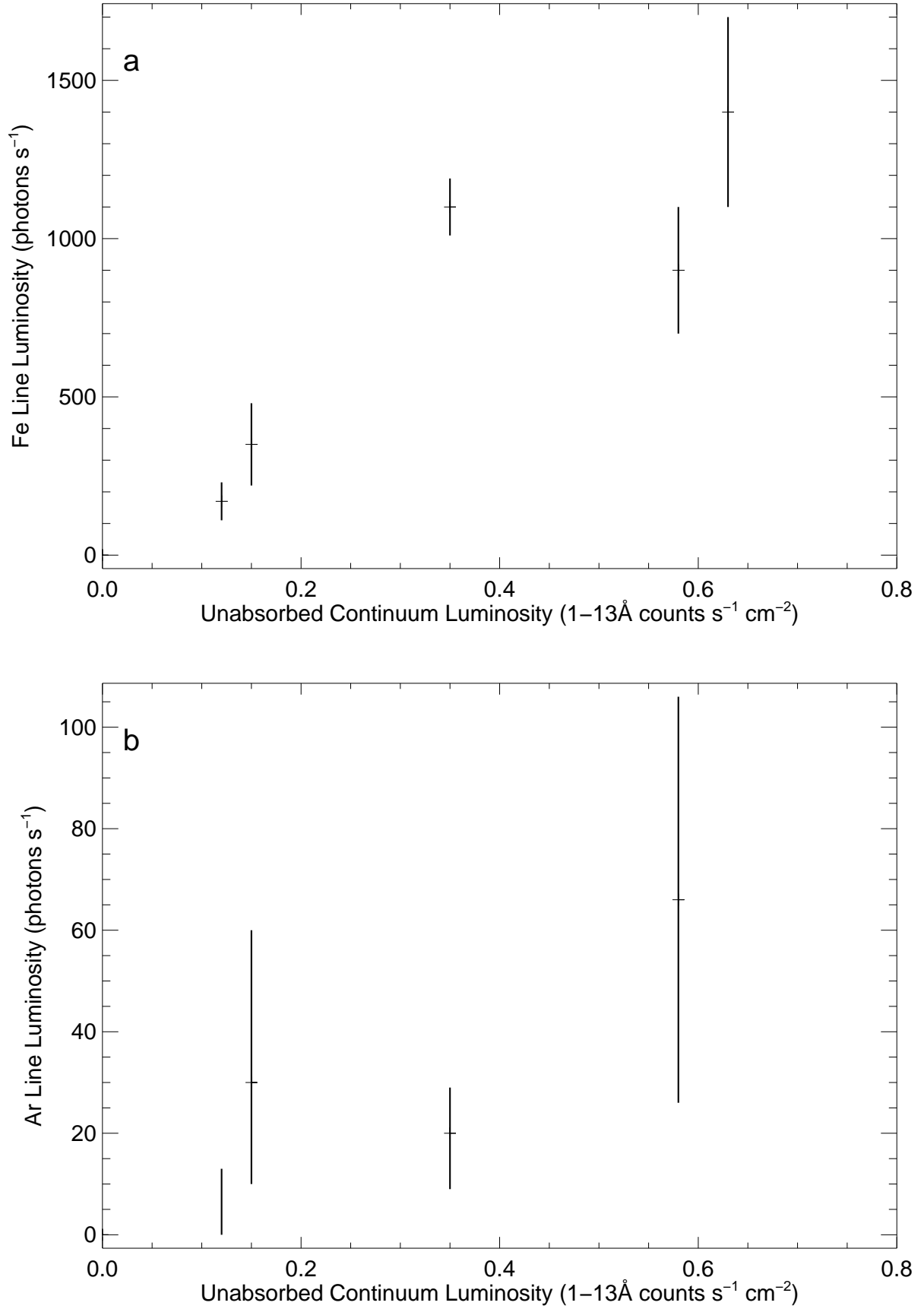
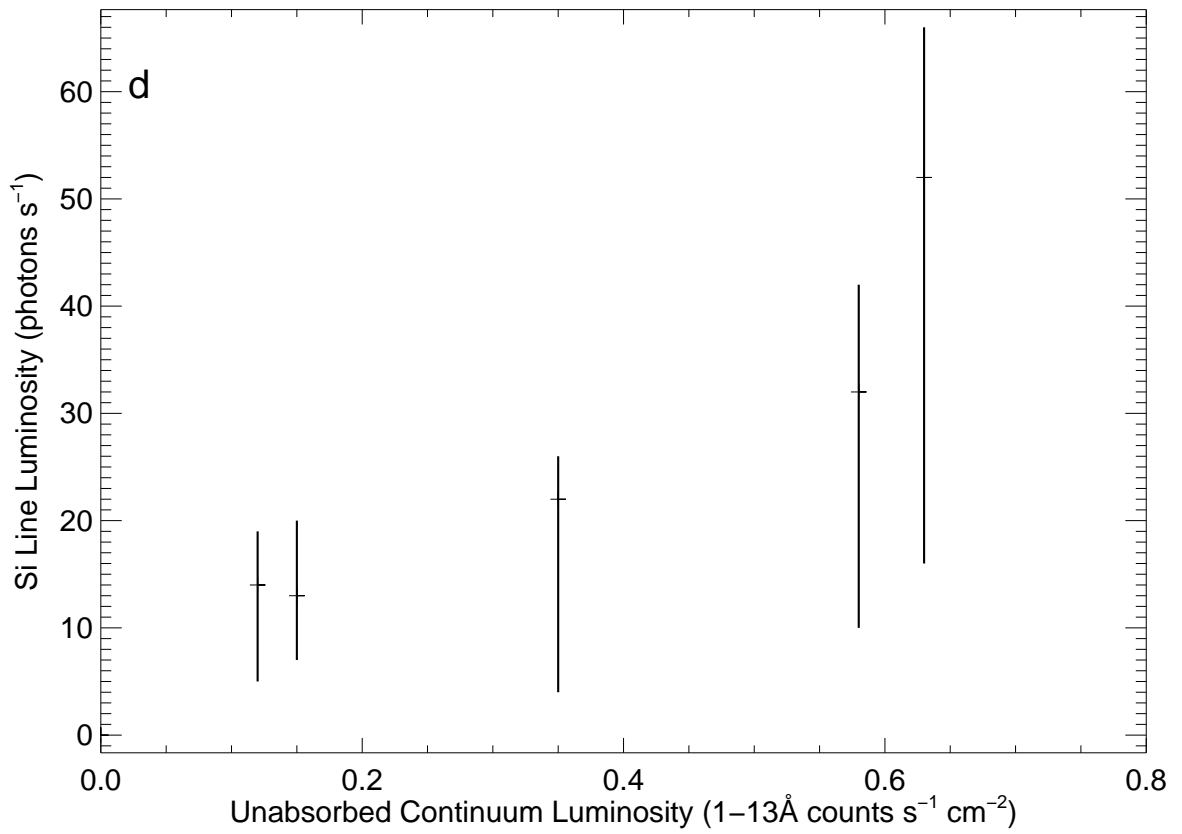
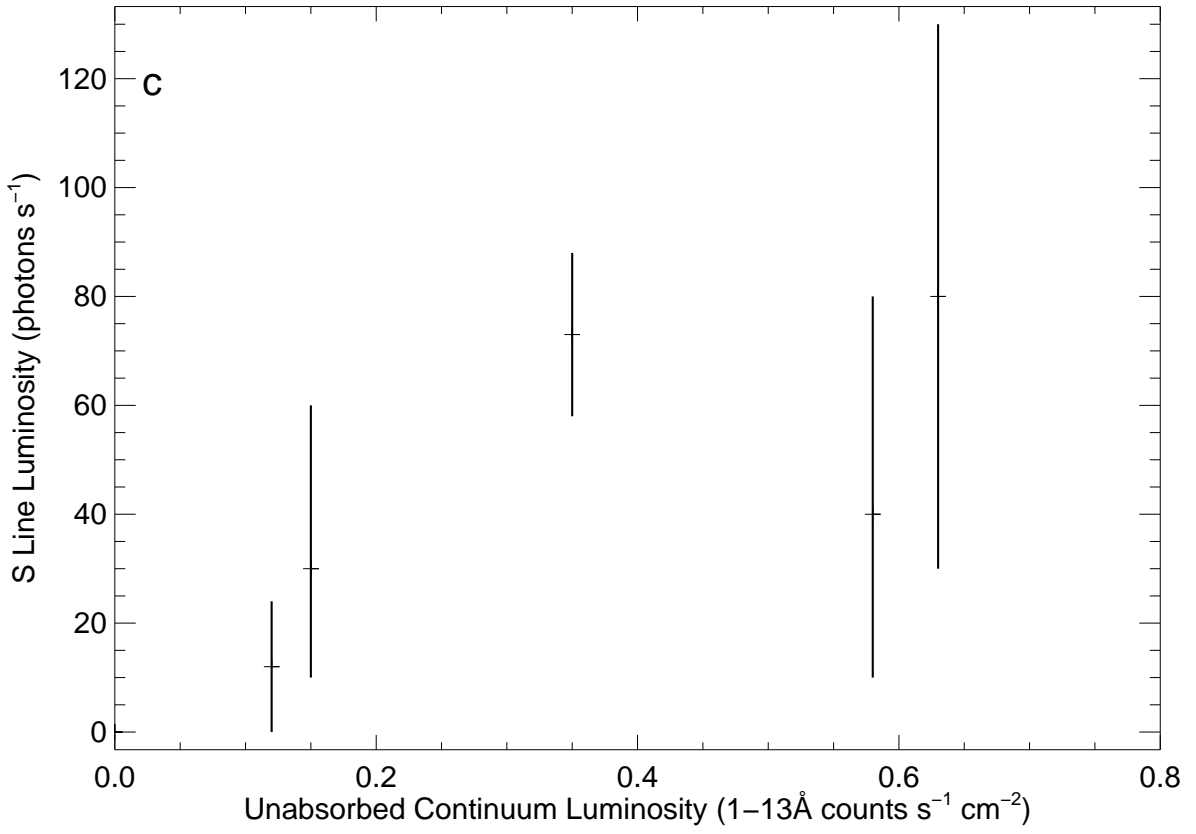
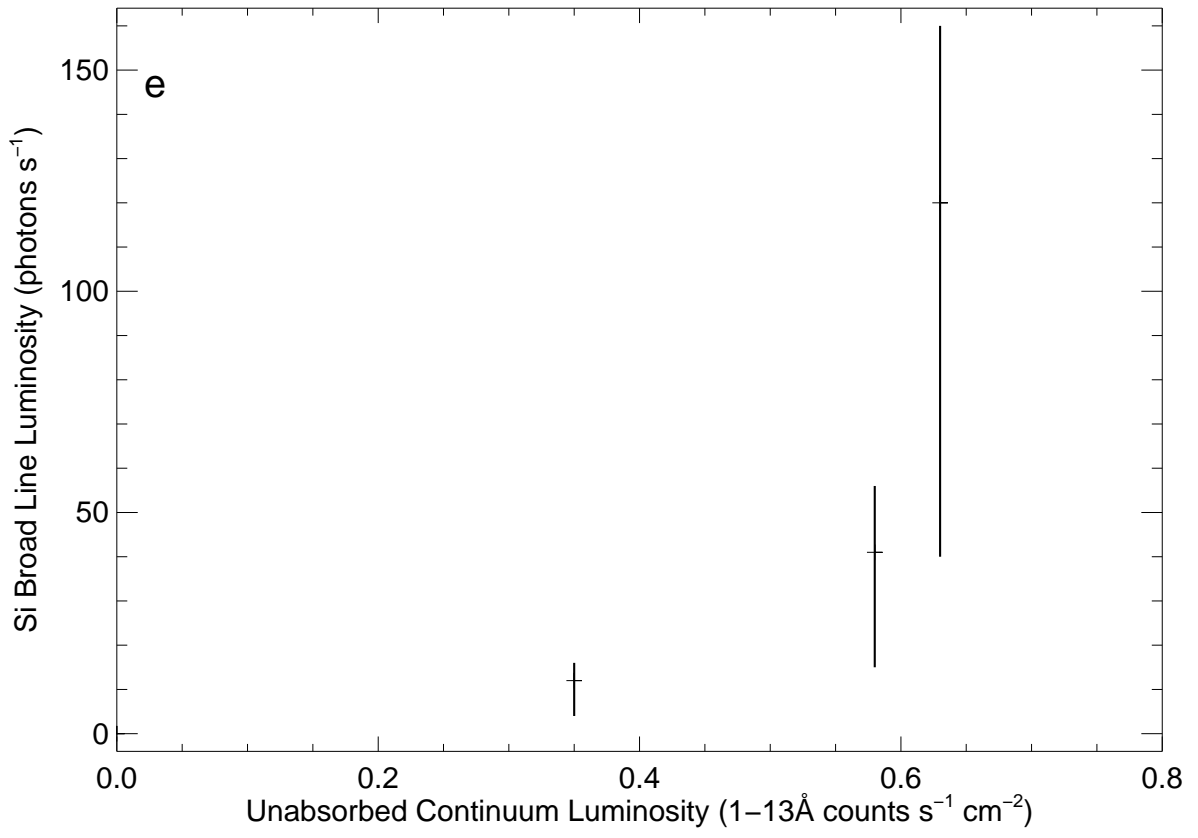


Fig. 7.—







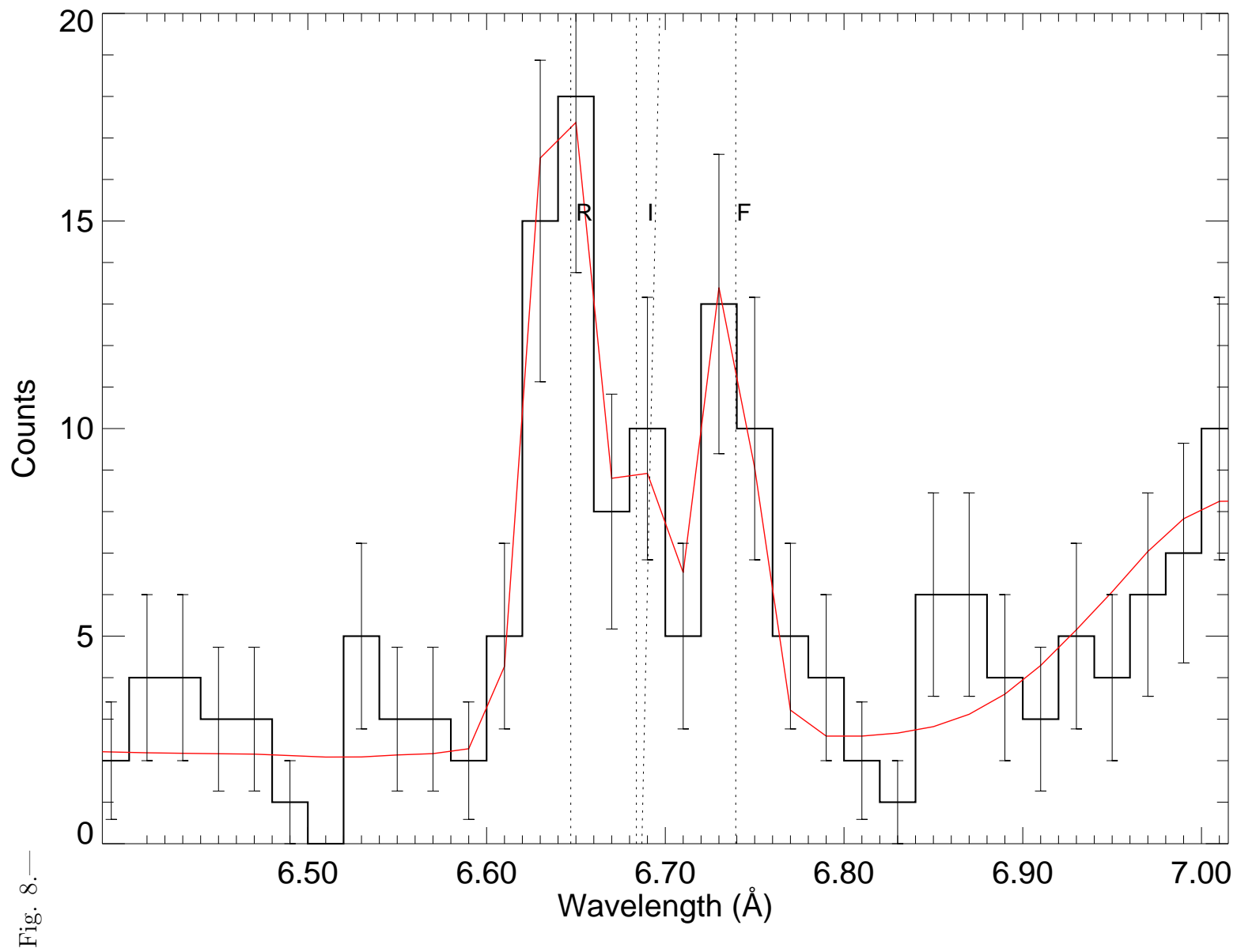


Fig. 8.—

Fig. 9.—

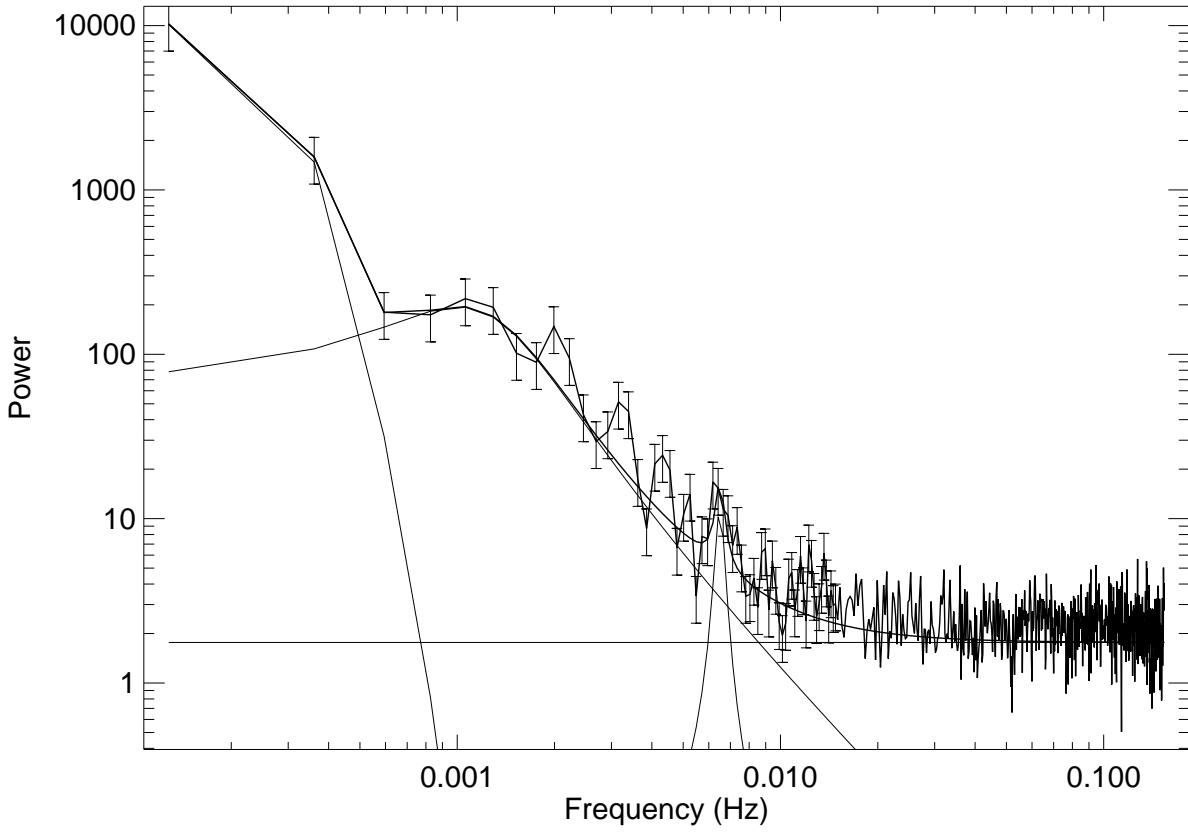


Fig. 10.—

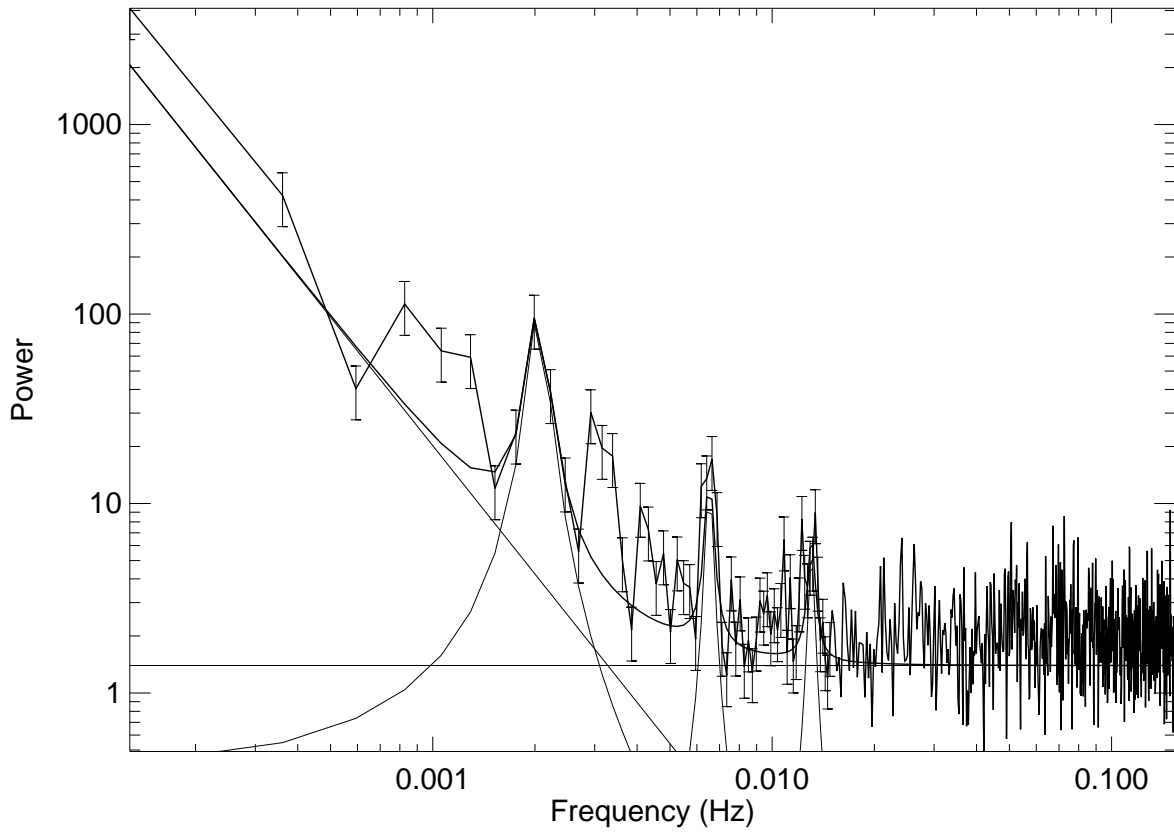


Fig. 11.—

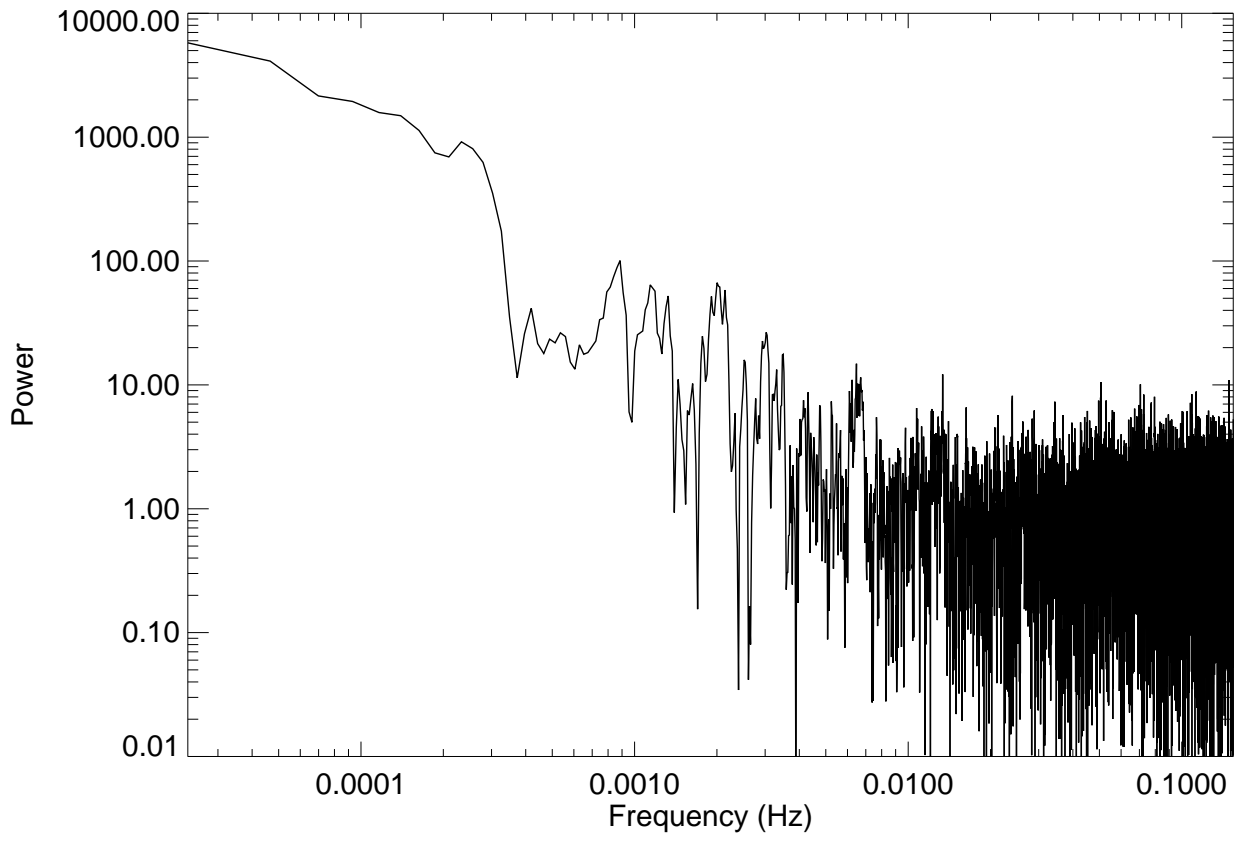


Fig. 12.—

